Benchmarking of three DWM-based wake models at below-rated wind speeds

Øyvind Waage Hanssen-Bauer[1], Paula Doubrawa[2], Helge Aa. Madsen[3], Henrik Asmuth[4], Jason Jonkman[2], Gunner C. Larsen[3], Stefan Ivanell[4], and Roy Stenbro[1]

[1]Institute for Energy Technology, Instituttveien 18, 2007 Kjeller, Norway
[2]National Renewable Energy Laboratory, Golden, CO 80401, USA
[3]Department of Wind Energy, Risø Campus, Technical University of Denmark, DK-4000 Roskilde, Denmark
[4]Wind Energy Division, Department of Earth Sciences, Uppsala University, 621 67 Visby, Sweden

Correspondence: Øyvind Waage Hanssen-Bauer (oyvind.hanssen-bauer@ife.no)

Abstract. Wind turbine wake models are essential tools for predicting power losses and structural loads in wind farms. Among these, the dynamic wake meandering (DWM) model, included as a recommended approach in the International Electrotechnical Commission design standard, is a widely used engineering-fidelity method that balances accuracy and computational cost. This study compares the performance of three DWM-based wake model implementations (from the Technical University of Denmark, the National Renewable Energy Laboratory, and the Institute for Energy Technology) under below-rated wind speed conditions. Model predictions of wake flow, power output, and structural loads for a four-turbine row are evaluated across different ambient turbulence levels and wind-direction misalignments, and compared against high-fidelity large-eddy simulation results. All three models captured the overall wake evolution and mean turbine performance with reasonable accuracy; their predicted time-averaged thrust and power were typically within 5–10 % of the large-eddy simulation benchmark. However, notable differences emerged in wake structure and unsteady load predictions, with discrepancies increasing for turbines further downstream. These differences highlight the importance of modelling choices such as wake summation and turbulence treatment, which strongly influence power-deficit and fatigue-load predictions. Comparison with large-eddy simulations reveals each approach's strengths and weaknesses, indicating where improvements are needed. Overall, the findings point to specific refinements for DWM models to improve their fidelity, ultimately enabling more robust wake predictions for wind farm design and operation.

1 Introduction

The wind energy industry has undergone significant development since its beginning, evolving from isolated, low-efficiency turbines to large-scale, modern wind farms. In these farms, spatial constraints and the need to minimize infrastructure and maintenance costs often lead to farm layouts with tightly spaced turbines. This evolution has increased the focus on turbine–turbine interactions, as wake effects have been identified as a major contributor to energy losses and elevated structural loads throughout the farm.

To maximize energy yield, the industry commonly employs simplified engineering models for steady-state wake prediction during design and operational planning. However, wakes from upstream turbines not only reduce wind speeds but also generate unsteady turbulence, which impacts the performance and fatigue loading of downstream machines. Because steady-state models are inherently unable to capture these unsteady flow phenomena, they are not suitable for load assessments. Instead, the industry commonly relies on the effective turbulence model (International Electrotechnical Commision, 2019) for structural load calculations, which does not simulate individual wakes explicitly but approximates their impact by artificially increasing the ambient turbulence intensity. The alternative approach to consider wake effects on turbine loads according to international wind turbine design standards is the dynamic wake meandering (DWM) model (Larsen et al., 2008; Madsen et al., 2010; Larsen et al., 2013). This approach explicitly simulates individual wakes as convecting, meandering flow fields, where the velocity deficit is advected downstream with stochastic lateral and vertical motion driven by ambient large-scale turbulence, superimposed on an ambient wind field. By capturing key unsteady wake dynamics such as meandering and advection, DWM-based models include physical phenomena that are absent from simpler steady-state models, yet remain orders of magnitude more computationally efficient than high-fidelity large-eddy simulations (LES). Recent work by Doubrawa et al. (2023) showed that even though the effective turbulence model and the DWM model predict similar intra-farm flow characteristics and, when coupled with aeroelastic solvers, turbine structural loads on average, much more insight and directional variability arise from the DWM model that the effective turbulence model cannot resolve. DWM models enable realistic load predictions under waked conditions – an essential capability for wind farm design and certification.

Since its introduction in the early 2000s, the DWM model has undergone continuous refinement. Several research groups have proposed enhancements or modifications to the original formulation, including alternative meandering algorithms, variations in wake-deficit shapes (Doubrawa et al., 2017; Branlard et al., 2023; Bernard et al., 2024), improved wake superposition techniques (Machefaux et al., 2016; de Vaal and Muskulus, 2021), and more advanced treatments of wake-added turbulence (Madsen et al., 2005; Keck et al., 2015; Branlard et al., 2024). These efforts have led to a range of DWM-based implementations, such as the original model integrated with DTU's aeroelastic software HAWC2, NREL's FAST.Farm tool (Jonkman et al., 2017), and the more recent WIFET wake model (Hanssen-Bauer et al., 2020; de Vaal and Muskulus, 2021), each incorporating unique sub-models. While grounded in the same core physical principles, their predictions can differ substantially due to implementation choices.

DWM-based models have been calibrated and compared with high-fidelity large-eddy simulations coupled with LES actuator-line turbine models (LES-ALM) (Madsen et al., 2010; Jonkman et al., 2018; Doubrawa et al., 2018; Shaler and Jonkman, 2021; Hanssen-Bauer et al., 2020) and also validated with full-scale field measurements (Madsen et al., 2010; Larsen et al., 2013, 2015, 2017). Direct intercomparisons between different DWM implementations remain limited, with a few notable exceptions. The benchmarking study by Asmuth et al. (2022) compared six numerical models – including DWM implementations from DTU and NREL, and the LES-ALM software Ellipsys3D – with full-scale measurements from the DanAero experiment. That study focused on a two-turbine setup under below-rated wind conditions, analyzing one full-wake and one partial-wake case. However, the scope was limited to the response of two turbines and the wake flow behind only the upstream rotor, leaving the effects of multiple interacting wakes unexamined. In another benchmarking study, Bernard et al. (2024) compared three

different DWM implementations, together with the effective turbulence model and LES, against measurement data from an offshore wind farm with 6 MW turbines located in the North Sea. This comparison presented the response of one turbine in the second row of the wind farm for below-rated wind speeds and different inflow directions, resulting in both free inflow and inflow partially affected by the wake of a single upstream turbine.

Our recent comparison of DWM-based models extended the benchmarking to an above-rated wind speed case, involving a four-turbine row aligned with the incoming wind and a single ambient turbulence condition (Hanssen-Bauer et al., 2023). That study revealed substantial discrepancies between the model implementations. While time-averaged wake deficits and power outputs were generally consistent across models and in reasonable agreement with LES, fatigue-load predictions diverged significantly further downstream, with differences reaching up to 25 $\%$ of reference values. These results underscore how implementation details, such as wake-merging methods and turbulence modelling, can critically affect load predictions, even under otherwise comparable conditions. They also highlight the need for continued evaluation and improvement of engineering-fidelity wake models before they can be fully relied upon in design and certification workflows.

In the present study, we extend the earlier above-rated comparison to systematically evaluate three DWM-based wake models under below-rated wind speed conditions, while introducing two further variables: ambient turbulence intensity and wind-direction misalignment. Specifically, we analyze three inflow conditions representative of low to moderately high turbulence environments and two wind alignment scenarios – one with flow aligned with the turbine row, resulting in a full-wake configuration, and another with a small offset angle introducing a partial-wake condition. A high-fidelity LES-ALM is used as the reference benchmark, following the methodology of our previous study (Hanssen-Bauer et al., 2023). This setup enables an in-depth assessment of wake evolution, power production, and structural load indicators along a row of turbines for each DWM model, across all combinations of wind speed, turbulence, and alignment.

The primary objectives of this study are twofold: (1) to evaluate each DWM model's accuracy relative to LES predictions, identifying deviations in wake behaviour and turbine fatigue response; and (2) to investigate how differences in sub-modelling strategies – such as wake meandering formulations, velocity-deficit profiles, multi-wake superposition methods, and wake-added turbulence treatments – affect model performance. By isolating and analyzing these factors, we aim to explain the observed differences and identify the most influential modelling assumptions, thereby informing future development of accurate, robust engineering-fidelity wake models for wind farm applications.

2 Methodology

In this study, we compare three different DWM-based wake models with high-fidelity LES-ALM. The original DWM model developed at the Technical University of Denmark (DTU) is referred to as $\mathrm{DWM_{DTU}}$. The second DWM model uses the National Renewable Energy Laboratory (NREL) DWM implementation in FAST.Farm, named $\mathrm{DWM_{NREL}}$ in this study. The third model, named $\mathrm{DWM_{IFE}}$, uses the DWM implementation WIFET Farm from the Institute for Energy Technology (IFE). This model is newly developed in the NEXTFARM project (RCN, 2025) and is an extension to the aeroelastic tool 3DFloat (Nygaard et al., 2016). The LES-ALM simulations were performed by Uppsala University and are hereafter called $\mathrm{LES_{UU}}$.

2.1 Test cases

In this study, we consider the same simple farm layout as in Hanssen-Bauer et al. (2023), a row of four NREL 5 MW reference turbines (Jonkman et al., 2009) spaced 7.5 diameters ($7.5D$) apart. The NREL 5 MW turbine has a rotor diameter of $D = 126$ m, a hub height of 90 m, a rated speed of 11.4 ms^{-1}, and a rated aerodynamic power of 5.3 MW. All numerical models, both DWM and LES, use the same incoming wind field, the LES-generated precursor described in Sect. 2.3. In this way, we exclude the effect of different inflow models and can investigate the differences in the wake models and their isolated impact on power and fatigue loads. However, an important exception is the computation of the meandering in the $\mathrm{DWM}_{\mathrm{DTU}}$ model, which is derived from a Mann turbulence box with a grid size of one diameter (Madsen et al., 2008, 2010). As this approach is an integrated part of the model and its calibrated parameters, we found it necessary not to deviate from this setup.

Three wind fields with varying ambient turbulence intensity (TI_{a}) were generated, representing low, medium, and high turbulence inflow conditions. Table 1 provides details about the flow at hub height for the different cases. While the aim was to have three wind fields with identical below-rated mean wind speed at hub height, in practice the mean wind speeds differ slightly. For the highest TI_{a} case, the mean wind speed is close to, but still below, the rated wind speed. The inflow data provided to the DWM models were sampled in a separate precursor run of the main LES without turbines, in a plane $1D$ upstream of the position of the most upstream turbine (hereafter referred to as turbine 1). This approach ensures that the inflows seen by the turbines are as similar as possible. For the DWM simulations, the LES-generated wind field was imposed $1D$ upstream of turbine 1, and the simulations were run for 52.5 min. To exclude transient effects at the beginning of the simulations, the first 7.5 min were discarded, resulting in an effective simulation length of $t_{\mathrm{sim}} = 45$ min. This corresponds to $6.7L_x/U_\infty \leq t_{\mathrm{sim}} \leq 8L_x/U_\infty$ for the different cases, where L_x is the longitudinal length of the flow domain, and U_∞ is the mean undisturbed ambient wind speed.

In total, four simulation cases were run in this study. Three cases had the mean wind direction aligned with turbine row but with varying inflow turbulence conditions, yielding fully waked configurations. Here, the turbines downstream of turbine 1 were operating in fully waked conditions. The fourth case was run with medium ambient turbulence conditions but with an offset angle of 5° between the mean wind direction and the turbine row, resulting in a scenario where turbines 2–4 operated under partially waked conditions. In all cases, the rotors were aligned with the mean wind direction (i.e. no intentional yaw misalignment). Due to an error in the setup of the LES-ALM simulation for the first case, the rotor was run with 0° tilt rather than the correct 5° tilt angle of the NREL 5 MW turbine. As the LES-ALM simulations are computationally expensive, it was decided to keep a 0° tilt angle for the first case and adjust the DWM simulations accordingly, while for the remaining cases the tilt angle was set to 5° (see table 1).

As in Hanssen-Bauer et al. (2023), the turbines were forced to operate at fixed rotor speeds and blade pitch angles in all simulations. These predefined values were set by first running the $\mathrm{DWM}_{\mathrm{IFE}}$ and $\mathrm{DWM}_{\mathrm{NREL}}$ models with variable rotor speed and blade pitch using the same inflow, then taking the mean of the time-averaged values from those runs for the final simulations. The resulting rotor speeds are given in table 1, while the blade pitch angles were 0° for all turbines, as expected for below-rated conditions. As described in Sect. 2.2.4, $\mathrm{DWM}_{\mathrm{DTU}}$'s approach for multiple-wake situations is to consider

Table 1. Inflow conditions at hub height, resulting pre-defined RPM values, and rotor tilt angle for the simulation cases

	U_{hub} $[\mathrm{ms}^{-1}]$	$\mathrm{TI}_{\mathrm{hub}}$ $[\%]$	RPM turbine 1 $[\mathrm{min}^{-1}]$	RPM turbine 2 $[\mathrm{min}^{-1}]$	RPM turbine 3 $[\mathrm{min}^{-1}]$	RPM turbine 4 $[\mathrm{min}^{-1}]$	Rotor tilt $[^\circ]$
Low $\mathrm{TI_a}$	8.86	4.6	10.23	8.43	8.36	8.35	0
Medium $\mathrm{TI_a}$	8.98	8.8	10.51	8.76	8.57	8.54	5
High $\mathrm{TI_a}$	10.63	12.0	11.86	10.76	10.44	10.38	5
Medium $\mathrm{TI_a}$/ Skewed inflow	8.98	8.8	10.36	9.40	9.32	9.27	5

the meandered wake deficit from each upstream turbine as if operating in isolation (i.e. experiencing free-stream velocity). The $\mathrm{DWM_{DTU}}$ approach thus differs from the other models by running all upstream wake-generating turbines at free-stream velocity, except for the turbine whose loads are being calculated. For example, when computing the loads of turbine 4, turbines 1 to 3 are set to the rotor speed given for turbine 1 in table 1, while turbine 4 is set to the RPM specified for that turbine.

To ensure comparability with the LES-ALM, we ran the aeroelastic solvers coupled to the DWM wake models with rigid rotors and excluded all tower effects. Aerodynamic forces, including gravity forces, along the blade span were output from all simulations, and power and loads were calculated from these forces using identical algorithms. This is the same procedure used in Hanssen-Bauer et al. (2023).

To compare fatigue-damage calculations for the different wake models, 45 min damage-equivalent loads (DELs) were calculated. Based on the Palmgren–Miner damage-summation rule with Goodman's correction, a DEL is a load that, at a chosen equivalent number of cycles – here $N_{eq} = 45 \cdot 60 = 2700$ (i.e. a load at 1 Hz for 45 min) – produces the same fatigue damage as the summation of damage from the K different load ranges S_k with N_k cycles, determined using rainflow counting (Rychlik, 1987):

$$\mathrm{DEL} = \left(\frac{1}{N_{eq}} \left(\sum_{k=1}^{K} N_k S_k^m \right) \right)^{\frac{1}{m}}, \tag{1}$$

where the material-specific Wöhler coefficient m in Eq. (1) is set to $m = 3$ for calculations on the tower and to $m = 10$ for the blade.

2.2 The DWM models

The original DWM model is based on the assumption that the quasi-steady wake deficit, obtained from a thin shear-layer approximation of the Navier–Stokes equations, meanders in a stochastic manner due to the large-scale turbulent structures in the wind, and that the self-generated turbulence field in the wake can be superimposed onto the wake deficit and exposed to the same dynamics. In this study, we compare three DWM-based wake models from DTU, NREL, and IFE. An overview of

the differences between these three DWM model implementations is given in Hanssen-Bauer et al. (2023). What follows is a summary of the most important differences needed to understand the discrepancies in the results.

2.2.1 Initial wake velocity deficit

$\mathrm{DWM_{DTU}}$ and $\mathrm{DWM_{NREL}}$ obtain the initial velocity profile behind the turbine from the blade element momentum (BEM) model (Madsen et al., 2008, 2010), but the wake profile is adjusted by including a simple closed-form modification to account for pressure recovery in the near-wake region. $\mathrm{DWM_{IFE}}$ on the other hand, assumes a Gaussian wake-deficit profile at all downstream positions, and the initial wake-centre deficit is obtained from $C_T(U)$ tables of thrust coefficient as function of wind speed for the specific turbine.

2.2.2 Thin shear-layer approximation and eddy viscosity model

All three DWM implementations build on the same assumption of an axisymmetric wake with a thin shear-layer approximation of the Navier–Stokes equations, where the pressure term is neglected. As a turbulence closure, an eddy viscosity model consisting of two terms is applied. The first term models the contribution related to the ambient wind shear and scales with the turbulence intensity, while the second term is related to the wake shear. The model includes filter functions to adjust the model in the near-wake region where the assumption of negligible pressure variations is not valid. The details of the eddy viscosity model, along with its associated filter functions and calibration constants, vary among the DWM implementations (for details, see Madsen et al., 2010; Jonkman et al., 2017; de Vaal and Muskulus, 2021).

2.2.3 Wake transport velocity

The wake deficit is transported downstream by the wind, but since the free-stream velocity is itself disturbed by the deficit, the choice of wake transport velocity is not trivial. $\mathrm{DWM_{DTU}}$ applies a transport velocity of U_∞, $\mathrm{DWM_{IFE}}$ uses the approximation $0.8U_\infty$, estimated by Keck et al. (2013). $\mathrm{DWM_{NREL}}$, on the other hand, calculates the local velocity at the position of each wake slice, which varies in both time and space; therefore, the wake accelerates from near-wake to far-wake, because the wake deficits are stronger in the near-wake and weaken further downwind.

2.2.4 Wake summation

For situations with multiple wakes, where a turbine's incoming flow field is affected by more than one upstream wake, $\mathrm{DWM_{DTU}}$ distinguishes between below- and above-rated wind speed conditions (Larsen et al., 2015):

$$U_w(x,y,z) = U_\infty - \begin{cases} \max_i \left(U_\infty - u_w^i(x,y,z)\right), & U_\infty \le U_\mathrm{r} \\ \sum_i (U_\infty - u_w^i(x,y,z)), & U_\infty > U_\mathrm{r} \end{cases} \tag{2}$$

Here, U_∞ is the undisturbed free-stream velocity, u_w^i is the wake velocity induced by turbine i, and U_r is the turbine's rated wind speed. In this study the wind speed is always below rated, so the upper expression is used. This maximum deficit operator

looks at the meandered wake deficit from each upstream turbine operating in isolation (i.e. under free-stream conditions), and assumes that the total incoming wake deficit can be approximated by the maximum single-wake deficit, evaluated at each radial position of the turbine of interest.

$\mathrm{DWM_{NREL}}$ superimposes axial velocity-deficits using a local root-sum-square method, where the wake of each turbine is calculated using that turbine's local incoming wind velocity. In other words, the wakes are calculated sequentially from upstream to downstream (Jonkman et al., 2017):

$$U_w(x,y,z) = U_\infty - \sqrt{\sum_i (u_0^i - u_w^i(x,y,z))^2} \tag{3}$$

Here, U_∞ is again the undisturbed free-stream velocity, u_0^i is the local incoming wind velocity at turbine i, and u_w^i is the wake velocity induced by turbine i.

Radial velocity-deficit fields are superimposed using a linear summation method in the same sequential manner as the axial component.

$\mathrm{DWM_{IFE}}$ uses the momentum-conserving summation method derived by Zong and Porté-Agel (2020a) for wake superposition. This is an iterative method in which the velocity deficits from the upstream turbines are summed with weights based on the ratio of each individual wake's mean convection velocity $u_c^i(x)$ to the combined wakes' convection velocity $U_c(x)$:

$$U_w(x,y,z) = U_\infty - \sum_i \frac{u_c^i(x)}{U_c(x)} (U_\infty - u_w^i(x,y,z)), \tag{4}$$

where

$$u_c^i(x) = \frac{\iint u_w^i(x,y,z) \cdot (u_0^i - u_w^i(x,y,z)) dydz}{\iint (u_0^i - u_w^i(x,y,z)) dydz}, \tag{5}$$

and

$$U_c(x) = \frac{\iint U_w(x,y,z) \cdot (U_\infty - U_w(x,y,z)) dydz}{\iint (U_\infty - U_w(x,y,z)) dydz}. \tag{6}$$

The integrals in Eqs. (5) and (6) are solved numerically over a cross-section with 64 grid points in each dimension, spaced $\Delta y = \Delta z = 10$ m apart and centred on the wake centre.

2.2.5 Tilt and yaw misalignment

The $\mathrm{DWM_{DTU}}$ and $\mathrm{DWM_{IFE}}$ implementations used in this study do not account for any flow effects due to tilt or yaw misalignment between the rotor and the flow. However, the latest version of $\mathrm{DWM_{DTU}}$ includes a model for flow effects due to yaw misalignment, using a Hill's vortex analogy (Larsen et al., 2020). By contrast, $\mathrm{DWM_{NREL}}$ accounts for tilt and yaw misalignments, which thereby influence wake deflection (Jonkman et al., 2017). The wake planes in the $\mathrm{DWM_{NREL}}$ model are oriented by the rotor centreline rather than the wind direction, causing the wake to deflect based on tilt and yaw misalignment because a wake deficit normal to the tilted/yawed rotor introduces a velocity component that is not parallel to the incoming flow. $\mathrm{DWM_{NREL}}$ also has a newly implemented curled-wake model with improved accuracy for large rotor misalignments (Branlard et al., 2023), but this extension is not used in the present study.

2.2.6 Ground effects

$\mathrm{DWM_{NREL}}$ does not yet have a model to account for ground effects on the flow field. Both $\mathrm{DWM_{DTU}}$ and $\mathrm{DWM_{IFE}}$ do include ground-effect models, but these were not used for the simulations in this study. In the case of $\mathrm{DWM_{IFE}}$, a mirror-based ground effect model was used in the simulations in Hanssen-Bauer et al. (2023), but it was later found to produce unrealistically high deficits near the ground. $\mathrm{DWM_{IFE}}$ showed better agreement when this model was turned off.

2.2.7 Wake-added turbulence and turbulence build-up

Wake-added turbulence is the self-generated small-scale turbulence in a turbine's wake due to wake shear and the breakdown of the wake tip vortices, and comes in addition to the conventional atmospheric boundary layer turbulence. Of the three DWM implementations, $\mathrm{DWM_{DTU}}$ is the only one including a wake-added turbulence model in the simulations performed for this study. In the early development of the DWM model at DTU, detailed inflow measurements on a full-scale turbine, including angle of attack and relative velocity at a blade section were used for validation. Comparisons between model simulations and these measurements made it clear that additional turbulence beyond that generated by wake meandering had to be modelled (Madsen et al., 2005). In practice, the wake's self-generated turbulence, particularly important under stable stratification of the atmospheric boundary layer, is modelled based on an isotropic Mann turbulence box with smaller length scale [1] than the ambient turbulence and transformed into an inhomogeneous turbulence field by a scaling factor k_{mt} that varies radially based on the wake-deficit strength and the wake shear-layer velocity gradient:

$$k_{mt} = \left|\frac{u_w(r)}{U_\infty}\right| k_{m1} - \left|\frac{\partial(u_w(r)/U_\infty)}{\partial r}\right| k_{m2}. \tag{7}$$

Here $k_{m1} = 0.6$ and $k_{m2} = 0.35$ are empirical factors tuned by comparison with inflow and load measurements on a full-scale turbine (Madsen et al., 2008) and with actuator-line simulations (Madsen et al., 2010). Later, an improvement to the original model to account for turbulence build-up inside a wind farm was suggested (Keck et al., 2015), but this is not included in the current $\mathrm{DWM_{DTU}}$ model.

The $\mathrm{DWM_{NREL}}$ results do not include any wake-added turbulence model in this study. However, an improved wake-added turbulence model has recently been implemented in FAST.Farm (Branlard et al., 2024).

$\mathrm{DWM_{IFE}}$ does not include a wake-added turbulence model for load calculations analogous to the one in the original DWM model. However, the increased turbulence intensity in the wake due to the turbulence-generating wake deficit shear is modelled through the eddy-viscosity formulation in the wake-deficit model, and the total contribution of increased turbulence from all upstream wakes is estimated by a root-sum-square summation (de Vaal and Muskulus, 2021). Thus, the increased effective turbulence intensity experienced by a turbine operating under waked conditions is taken into account and affects the development of its own wake downstream. Note that this summation of turbulence contributions from upstream wakes differs from the momentum-conserving method in Eq. (4) used for summation of the velocity deficits.

[1] $L = D/8$, where L is the length scale of the spectral velocity tensor and D is the turbine diameter, as opposed to $L = 33.6$ m, which is recommended for atmospheric turbulence above 60 m (International Electrotechnical Commision, 2019).

2.2.8 Aeroelastic solvers

All DWM models are coupled to an aeroelastic solver for calculating blade forces. $\mathrm{DWM_{DTU}}$ is coupled to HAWC2 (Madsen et al., 2020), $\mathrm{DWM_{NREL}}$ to OpenFAST (NREL, 2025), and $\mathrm{DWM_{IFE}}$ to 3DFloat (Nygaard et al., 2016). In all these aeroelastic solvers the blade forces are obtained from BEM, although in different implementations, with Prandtl blade tip correction (Glauert, 1935). $\mathrm{DWM_{NREL}}$'s OpenFAST additionally includes a blade-root correction.

2.3 Large-eddy simulations

The LES-ALM reference case ($\mathrm{LES_{UU}}$) as well as the three inflow wind fields used by all numerical models in this study, are computed using the EllipSys3D numerical framework (Michelsen, 1994a, b; Sørensen, 1995), and is identical to the solver used in our above-rated comparison (Hanssen-Bauer et al., 2023). This solver also participated in the aforementioned benchmarking study against full-scale measurements (Asmuth et al., 2022), although under the name LES-EllipSys3D or $\mathrm{LES_{DTU}}$.

The three inflow wind fields are generated using a bi-periodic precursor simulation of a pressure-driven isothermal boundary layer. The computational domain extends $L_z = 1280\ \mathrm{m}$ in the vertical direction, $L_x = 6L_z$ in the streamwise direction, and $L_y = 4L_z$ in the lateral direction. The grid is uniform in all coordinate directions, with $\Delta x = 20\ \mathrm{m}$ and $\Delta y = \Delta z = 10\ \mathrm{m}$. A symmetry boundary condition is imposed at the domain top. At the surface, shear stress is prescribed using Monin-Obukhov similarity theory (Monin, 1954) and the local instantaneous velocity sampled at the first grid point above the boundary. Inflow data for the main LES-ALM simulation, which are also used by the DWM models, are extracted after a spin-up time of 30 000 s.

The domain of the $\mathrm{LES_{UU}}$ simulation (including wind turbines) has the same dimensions $L_{x,y,z}$ as the precursor. The inlet is located $6D$ upstream of turbine 1. In the turbine and wake region, the grid is uniform with a resolution of $\Delta x = \Delta y = \Delta z = D/32 = 3.9375\ \mathrm{m}$, starting $3D$ upstream of turbine 1 and extending $33D$ in the streamwise direction, and $4D$ in both the lateral and vertical directions. Outside this inner region, the grid is smoothly stretched towards the boundaries. The turbine rotors are represented using ALMs (Sørensen and Shen, 2002), with each blade discretized into 32 elements. The ALM body forces are projected onto the grid with a three-dimensional Gaussian smearing function of width $\epsilon = 2\Delta x$. To mitigate spurious induction effects arising from the finite core size of root and tip vortices, the smearing correction proposed by Meyer Forsting et al. (2019) is applied. Following a spin-up of $30\ \mathrm{min}$, the main simulation is run for $45\ \mathrm{min}$.

2.4 Wake tracking

From the flow field generated by $\mathrm{LES_{UU}}$, wake centre positions were tracked using NREL's Python toolbox SAMWICh. The wake centres were identified for each time step in a plane $5D$ downstream of each turbine (normal to the wind-direction) using the two-dimensional Gaussian fit method (Trujillo et al., 2011) as implemented in SAMWICh. To minimize algorithm error, the search area was limited to $\pm 1.25D$ laterally from the turbine location, and between $-0.5D$ and D vertically relative to hub height. After obtaining the wake centre time series for each turbine and downstream location, four post-processing steps were applied to reduce error in the wake centre estimates. These post-processing steps were determined based on a separate analysis

of $\mathrm{DWM_{NREL}}$ simulation results, where SAMWICh wake centre detections were compared to actual wake centre values output directly from $\mathrm{DWM_{NREL}}$:

1. Edge Detection Removal: wake centres detected at the edge of the search area were discarded and filled in by linear interpolation.

2. Spike Removal 1: a median filter with a kernel size of 15 s was applied to remove spurious spikes in the wake centre time series.

3. Jump removal: to remove remaining jumps in the wake centre time series, a moving average was applied to segments starting 20 s before the first and 20 s after the last consecutive points exceeding a maximum allowable gradient of $0.2D$ s^{-1}.

4. Spike Removal 2: a final median filter (identical to step 2) ensured that any spikes introduced by step 3, primarily due to the arbitrary selected segment length, were reduced in the post-processed wake centre time series.

Despite the improvements after post-processing the raw wake centres, the SAMWICh-derived centres did still at times differed from the centres computed by $\mathrm{DWM_{NREL}}$. This discrepancy could occur because SAMWICh tracks the aggregate deficit made up of more than one wake deeper in the farm. The difference between the standard deviation of the wake centre time series tracked by SAMWICh and that obtained directly from $\mathrm{DWM_{NREL}}$ remained below $0.06D$ (i.e. 6 $\%$ of the rotor diameter) for all inflow cases and for both lateral and vertical wake centre coordinates.

3 Results

3.1 Fully waked cases with varying ambient turbulence

In this section, we present a detailed comparison of the three DWM-based models under fully waked conditions for a row of four turbines exposed to aligned inflow. Three cases corresponding to low, medium, and high ambient turbulence conditions are considered, while maintaining below-rated wind speeds. We assess time-averaged flow fields, wake centre positions, power production, thrust forces, blade loads, and fatigue to identify key differences between the models and examine the influence of sub-modelling strategies.

3.1.1 Mean velocity profiles

Figure 1 shows time-averaged velocity profiles at $-1D$, $2.5D$, and $5D$ relative to the four turbines' streamwise positions for the low ambient turbulence case ($\mathrm{TI_a}$ = 4.6 $\%$). The upper row shows horizontal profiles at hub height and the lower row shows vertical profiles at the turbines' lateral centre. Horizontal dashed lines indicate the range of the turbine's rotor-swept area. In the near wake of turbine 1 at $x_{t=1} = 2.5D$, all models except $\mathrm{DWM_{IFE}}$ show velocity profiles with two minima reflecting the rotor thrust distribution. For $\mathrm{DWM_{DTU}}$, this characteristic near-wake profile is more pronounced than the LES profile, with lower

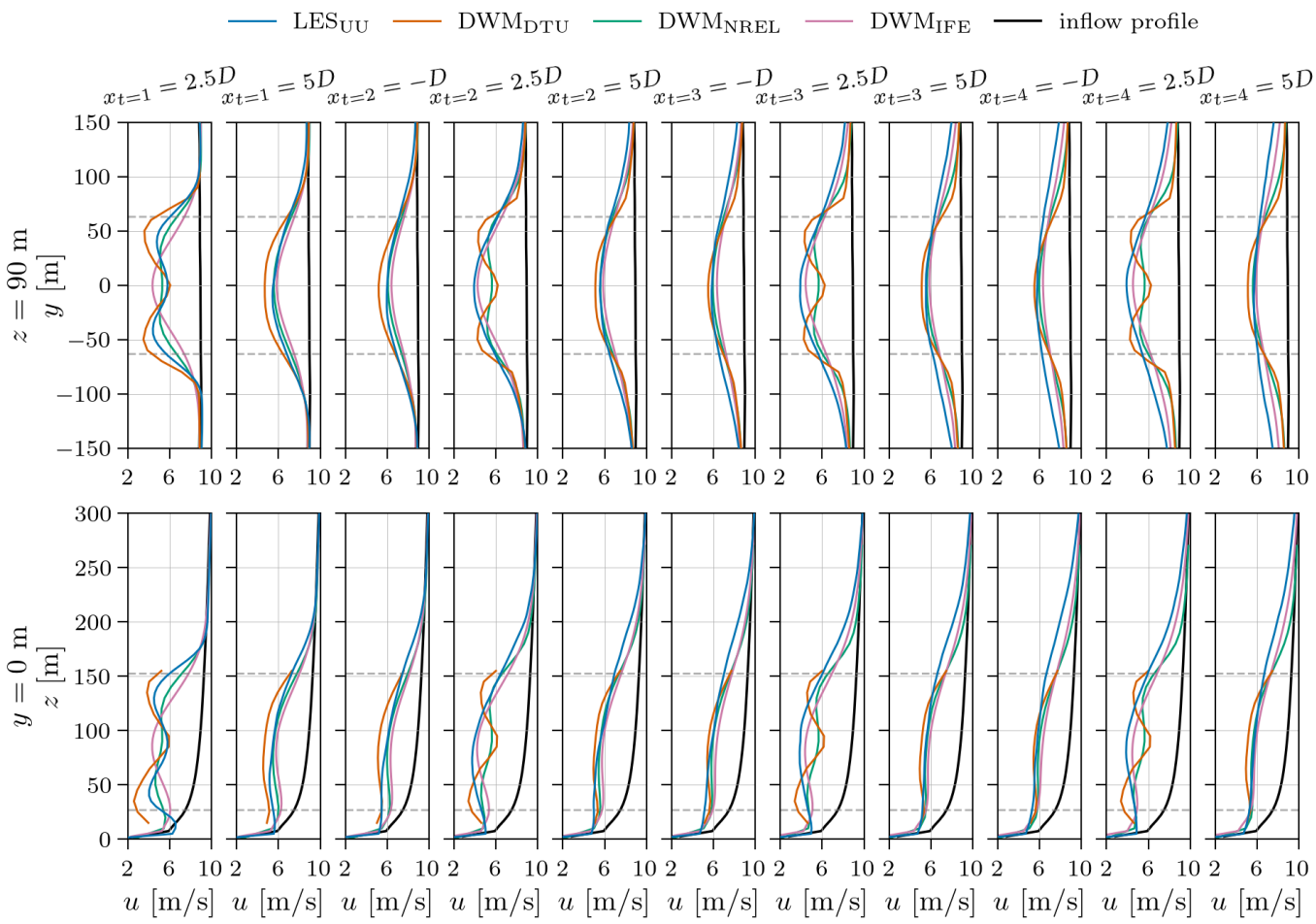

Figure 1. Time-averaged velocity profiles for the aligned incoming wind case with low ambient turbulence (TI_a = 4.6 %). Horizontal dashed lines indicate the rotor swept area.

velocities at the minima and higher velocity near the hub height, whereas the opposite is true for DWM$_{NREL}$. Both DWM$_{DTU}$ and DWM$_{NREL}$ predict the initial velocity profile downstream of the turbine using the BEM model. DWM$_{IFE}$, by contrast, assumes a Gaussian wake-deficit profile for all x downstream of the turbine. For LES$_{UU}$, DWM$_{DTU}$, and DWM$_{NREL}$, the velocity-deficit profiles have nearly reached a Gaussian-like shape by $x_{t=1} = 5D$. While all models show similar shapes for the horizontal profiles at $x_{t=1} = 5D$ and $x_{t=2} = -D$, the vertical profile of LES$_{UU}$ differs slightly in shape from the others, with relatively larger deficits at the lower part of the rotor swept area compared to the upper. For turbines 2–4, both DWM$_{NREL}$ and DWM$_{DTU}$ estimate the transition from BEM to Gaussian shape later than LES$_{UU}$, which already shows a Gaussian profile at $x = 2.5D$. While the DWM models show symmetric horizontal velocity deficits for the developed profiles, the LES$_{UU}$ deficit has its maximum at $y < 0$. This small asymmetry in LES$_{UU}$, which becomes more pronounced for higher ambient turbulence

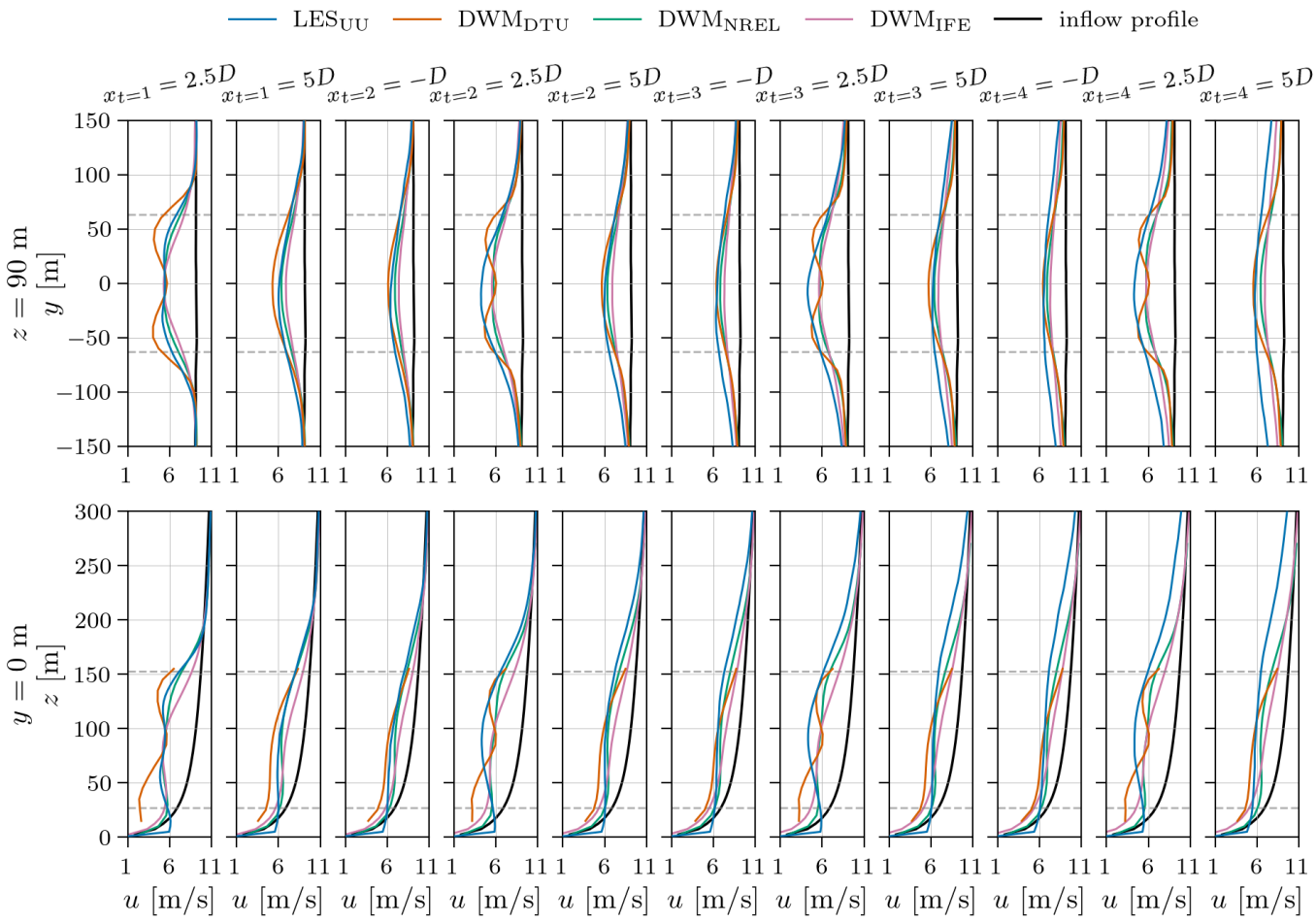

Figure 2. Time-averaged velocity profiles for the aligned incoming wind case with medium ambient turbulence (TI_a = 8.8 %). Horizontal dashed lines indicate the rotor swept area.

cases, will be discussed in Sect. 3.1.2 when wake centre positions are presented. At the wake centre, DWM$_{IFE}$ generally tends to underpredict the deficit slightly compared to LES$_{UU}$. DWM$_{NREL}$ shows good agreement with LES$_{UU}$ at the wake centre at $x = 5D$ and $x = -D$, while DWM$_{DTU}$ tends to slightly overpredict the centreline deficit at these positions.

DWM$_{DTU}$ and DWM$_{NREL}$ show only minor differences in the flow downstream of turbines 2–4 compared to turbine 1. By contrast, the wakes of DWM$_{IFE}$ and LES$_{UU}$ show significant development as the deficit outside the rotor swept area increase along the row of turbines. Hence, DWM$_{IFE}$ and LES$_{UU}$ show lower velocity gradients in the wake shear layer between the deficit and the ambient flow for all waked turbines, especially for turbine 4, compared to DWM$_{DTU}$ and DWM$_{NREL}$. The momentum-conserving wake summation method in DWM$_{IFE}$ (Eq. (4)) seems to capture the impact of far-upstream wakes, which have expanded over a long distance, but still produces weaker deficits towards the sides and above the rotor compared to

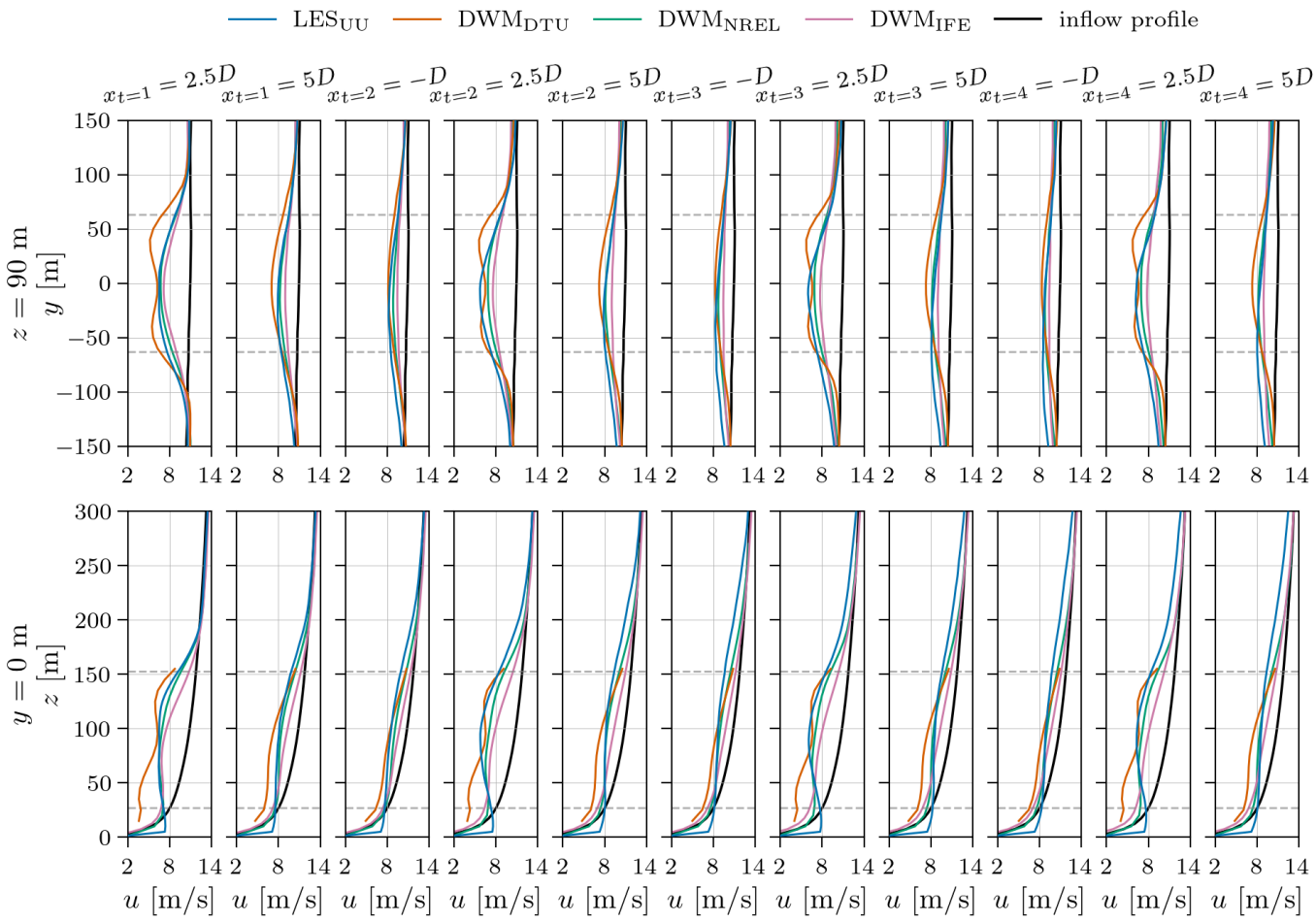

Figure 3. Time-averaged velocity profiles for the aligned incoming wind case with high ambient turbulence (TI_a = 12 %). Horizontal dashed lines indicate the rotor swept area.

LES$_{UU}$. By contrast, the wake-deficit profiles predicted by DWM$_{DTU}$ and DWM$_{NREL}$ show less lateral and vertical spreading. The maximum-deficit operator in the DWM$_{DTU}$ model derives the incoming deficit at each radial position as the smallest deficit found among all upstream turbines' meandered deficits (see Eq. (2) and Larsen et al. (2013)). This causes DWM$_{DTU}$ to predict only small variations in the incoming velocity field for turbines 2–4, resulting in similar wake profiles along the row. The fact that DWM$_{NREL}$ predicts only minor variations in the wake flow for turbines 2–4 is more surprising given the sequential multi-wake handling in this model (see Eq. (3)). However, the closer agreement of DWM$_{IFE}$ with LES$_{UU}$ in predicting wake development along the turbine row may also stem from DWM$_{IFE}$ being the only DWM implementation that incorporates a turbulence build-up model. This model accounts for the elevated incoming turbulence levels experienced by turbines 2–4 due

to added turbulence in upstream wakes, leading to faster wake recovery through enhanced mixing and momentum entrainment from the ambient flow.

Figures 2 and 3 show time-averaged velocity profiles for the medium (TI_a = 8.8 %) and high (TI_a = 12 %) ambient turbulence cases, respectively. The wake development behind each turbine is similar to the low-turbulence case, but higher turbulence levels and thus stronger meandering, lead to faster wake recovery and a quicker transition toward Gaussian profiles. As in the low-turbulence case, DWM_{DTU} shows a more distinct near-wake profile than the other models at $x = 2.5D$ for all turbines and for both TI_a = 8.8 % and TI_a = 12 %. Under medium ambient turbulence, only traces of the characteristic near-wake profile are visible in the wakes of DWM_{NREL} and LES_{UU} (evident at $x = 2.5D$ downstream of all turbines for DWM_{NREL}, and only at $x_{t=1} = 2.5D$ downstream of turbine 1 for LES_{UU}). For the high ambient turbulence case, the wakes predicted by both DWM_{NREL} and LES_{UU} have developed to Gaussian profiles by $x = 2.5D$ behind all turbines. It should be noted, however, that for power and load predictions the near-wake at $x = 2.5D$ has minor importance.

More relevant are the profiles at $x = 5D$ downstream and $x = -D$ just upstream the next turbine in the row. Here, DWM_{IFE}, and to a lesser degree DWM_{NREL}, tends to underpredict the centreline deficit, while DWM_{DTU} slightly overpredicts the deficit, compared to LES_{UU}. As in the TI_a = 4.6 % case, DWM_{IFE} is the only DWM model that captures the increase in deficit outside the rotor span in the horizontal profiles along the turbine row, although not to the same extent as LES_{UU}. For the vertical profiles, however, DWM_{IFE} does not show such an increase along the row. Again, DWM_{DTU} and DWM_{NREL} show only minor development in the flow along the turbine row, when comparing the wakes of turbine 1 and turbine 2 and especially when comparing the wakes of turbines 2–4.

LES_{UU} shows some notable differences in the flow field as the ambient turbulence level increases: as mentioned, the asymmetry about $y = 0$ becomes more pronounced for higher ambient turbulence, and a strong acceleration of the flow appears near the surface behind all turbines. In addition, the wake moves slightly upward, noticeable behind turbine 2 and further downstream. This upward deflection is likely due to the non-zero turbine tilt angle for the TI_a = 8.8 % and TI_a = 12 % cases, which causes the wakes to deflect upwards. DWM_{NREL} is the only DWM model that accounts for rotor tilt when calculating the flow. Even though an upward wake deflection is not evident for DWM_{NREL} in the velocity profiles, it becomes visible in the wake centre position plots in Sect. 3.1.2.

Figures 4–6 show profiles of axial velocity standard deviation, σ_u, for the three ambient turbulence levels. In general, LES_{UU} exhibits much higher σ_u levels than DWM_{NREL} and DWM_{IFE}. DWM_{DTU}, however, the only DWM implementation in this study that includes a wake-added turbulence model, shows comparable levels to LES_{UU} at TI_a = 8.8 %, and even higher at TI_a = 12 %. For all ambient turbulence levels, the shapes of DWM_{DTU}'s σ_u profiles downstream of turbine 1 are in fairly good agreement with LES_{UU} except near the surface. This deviation from LES_{UU} could stem directly from the wake-added turbulence formulation, but also from differences in predicted wake shape, since the wake shape affects the wake-added turbulence via the velocity gradient. The instantaneous wake shape also impacts σ_u in all models through wake meandering, since areas with higher velocity gradients in the wake experience larger temporal velocity fluctuations as the wake meanders. Deeper into the farm, it becomes clear that the absence of a turbulence build-up model in DWM_{DTU}, as addressed in Keck et al. (2015) and Branlard et al. (2024), amplifies the differences along the turbine row. Even though not including a wake-added

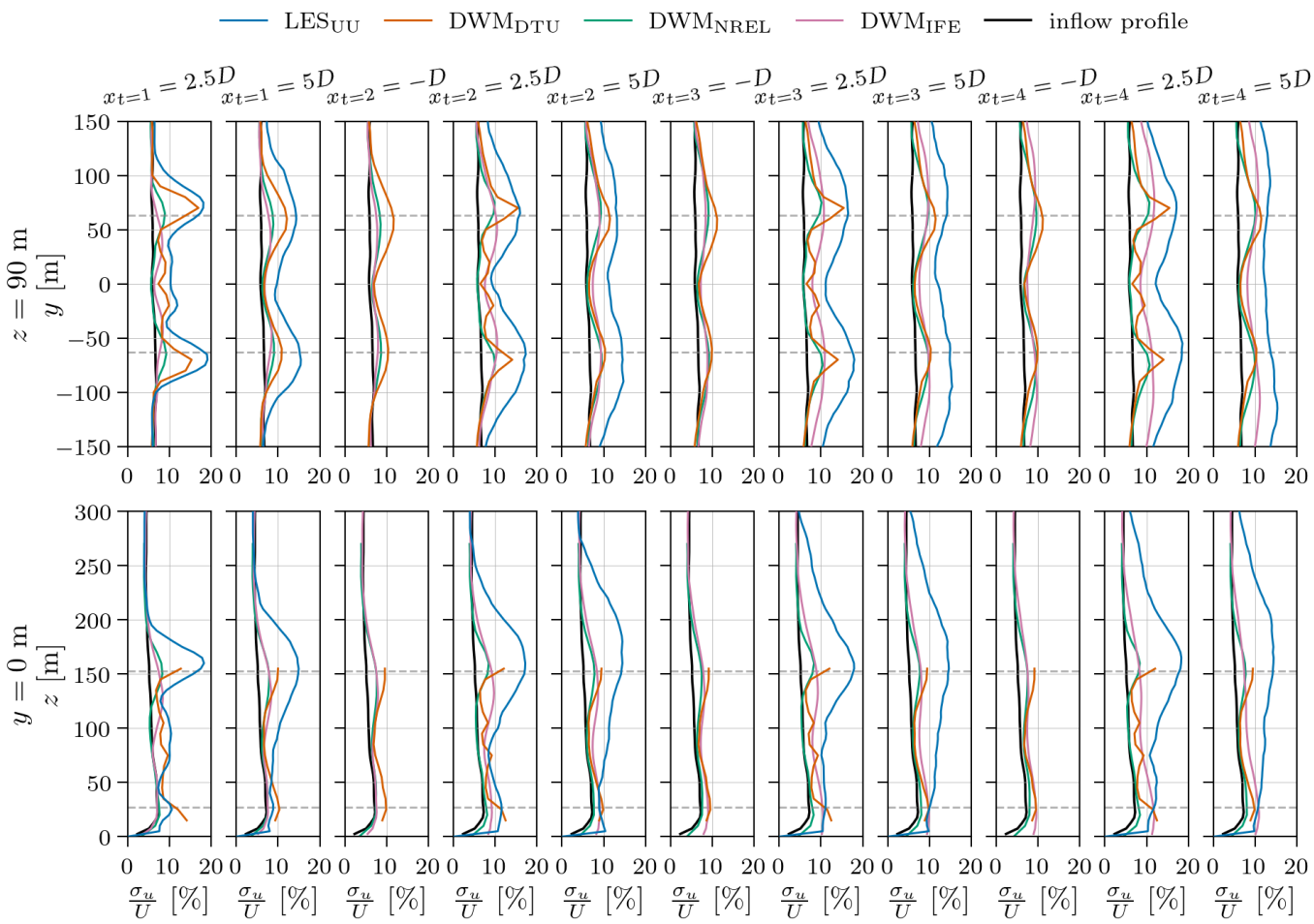

Figure 4. Profiles of velocity standard deviation for the aligned incoming wind case with low ambient turbulence (TI_a = 4.6 %). Horizontal dashed lines indicate the rotor swept area. LES_{UU} data are not available at $x_{t=i} = -D,\ i = 2, 3, 4$ due to lack of time-resolved data at this axial position.

turbulence model, the DWM_{IFE} implementation includes a model for turbulence build-up. This is evident in the low ambient turbulence case shown in Fig. 4, where σ_u levels in DWM_{IFE} increase along the row and approach those of LES_{UU} in the wake of turbine 4. This increase is not observed in Figs. 5–6, possible because the ambient turbulence is already high in those cases, making the relative wake turbulence build-up smaller.

3.1.2 Wake centre positions

Figures 7 and 8 show distributions of horizontal and vertical wake centre positions relative to the hub positions, at axial positions $5D$ downstream of each turbine in the row, under low and high ambient turbulence conditions (the medium ambient

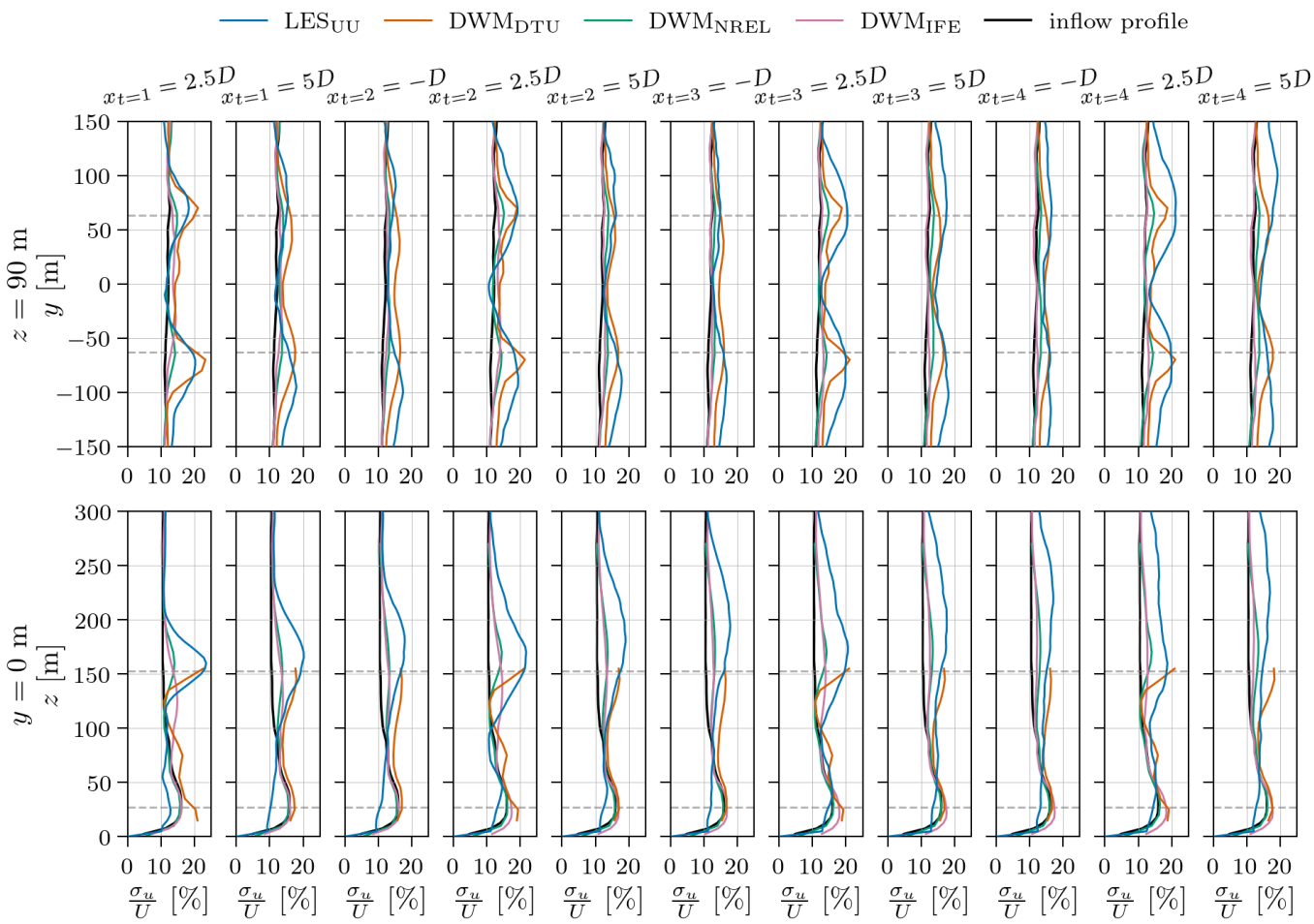

Figure 5. Profiles of velocity standard deviation for the aligned incoming wind case with medium ambient turbulence (TI_a = 8.8 %). Horizontal dashed lines indicate the rotor swept area.

turbulence case is shown in Fig. A3 in Appendix A). The distributions are shown as box-and-whisker plots, where the box spans the first and third quartiles and the orange line within the box denotes the median wake centre position. Whiskers extend to the most extreme non-outlier data point, and outliers, shown as circles, are defined as points outside the box beyond 1.5 times the box size ($1.5(Q_3 - Q_1)$). For those models labelled with a subscript "S", the wake centres were tracked using NREL's SAMWICh toolbox, described in Sect. 2.4. For the other models, wake centres come directly from each DWM model's own meandering algorithm. For DWM$_{NREL}$, we show both the wake centres from SAMWICh and directly from DWM, to illustrate differences between these two approaches.

At TI_a = 4.6 % all models predict the median wake centre of turbine 1 to remain near the hub position, (0,0) in the plots. In this low ambient turbulence case, the turbines are modelled with zero rotor tilt. The DWM models similarly keep the median

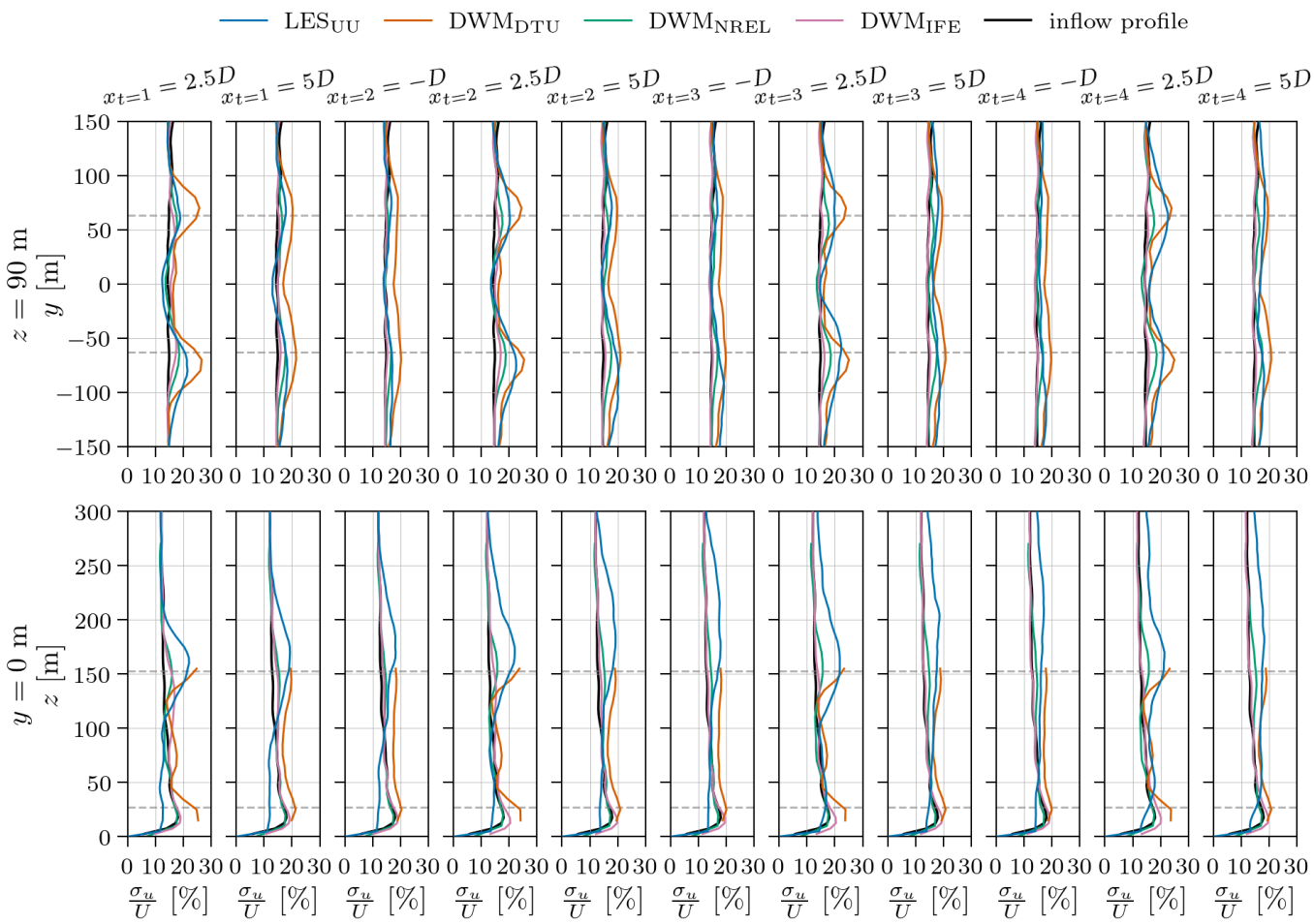

Figure 6. Profiles of velocity standard deviation for the aligned incoming wind case with high ambient turbulence (TI_a = 12 %). Horizontal dashed lines indicate the rotor swept area.

wake positions of turbines 2–4 near (0,0), whereas in LES$_{UU}$ the wakes shift slightly upward and to the right (negative y) further down the turbine row. At TI_a = 12 %, the trends are similar, except that the LES$_{UU}$ wake moves further upwards, and the DWM$_{NREL}$ wake also shifts slightly above hub height. In the TI_a = 12 % case the turbines were operated with a 5° rotor tilt. Notably, any misalignment of the rotor with the inflow is known to deflect the wake (Clayton and Filby, 1982), so a positive tilt is expected to deflect the wake upward. DWM$_{NREL}$ is the only DWM model that accounts for wake deflection from tilt or yaw misalignment, which is reflected in the results. At TI_a = 12 %, the median positions of the wake centres clearly shift to the right (negative y) with downstream distance for all models except DWM$_{DTU}$, where the meandering is driven by a separate Mann box and not by the LES inflow. The LES precursor has a small mean y-velocity component of -0.23 ms^{-1} at hub position for the TI_a = 12 % case. If the wakes simply advected with this lateral velocity like passive tracers, they would

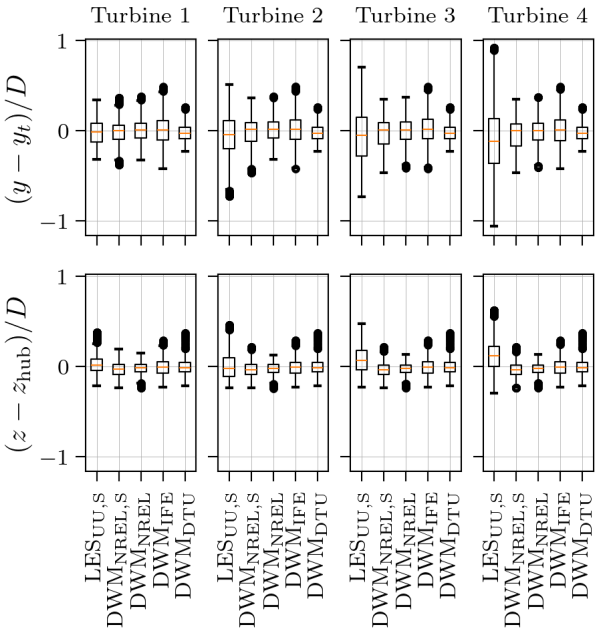

Figure 7. Box plots of horizontal (upper row) and vertical (lower row) wake centre positions at $x = 5D$ behind the turbines, for the aligned incoming wind case with low ambient turbulence ($\mathrm{TI_a}$ = 4.6 %).

move about $\sim -17\mathrm{m} \sim -0.13D$ in y direction at $5D$ downstream. This is on the same order as the median wake displacements predicted by the DWM models at $5D$ downstream for all turbines, and thus likely explains the slight lateral asymmetry seen in those cases. By the same reasoning, a mean vertical velocity of -0.076 ms^{-1} in the inflow would move the wake centre by $\sim -0.043D$ over $5D$. This is in the same order as the upward shifts predicted by $\mathrm{DWM_{DTU}}$ and $\mathrm{DWM_{IFE}}$, whereas $\mathrm{LES_{UU}}$ and $\mathrm{DWM_{NREL}}$ show upward deflection since the contribution from rotor tilt is dominating.

In $\mathrm{LES_{UU}}$, the wakes show a horizontal displacement in all cases: the largest in the high turbulence case, consistent with the -0.23 ms^{-1} mean y-velocity, but even in the low and medium turbulence cases where the mean y-velocity are near zero (0.0126 and -0.0710 ms^{-1}, respectively). These asymmetries in the $\mathrm{LES_{UU}}$ flow becomes more pronounced further down the turbine row. Notably, even without any rotor misalignment between the rotor and the incoming wind, wake deflections have been observed previously in both experiments (Bartl et al., 2018; Bossuyt et al., 2021) and LES studies (Fleming et al., 2014). As explained in detail by Zong and Porté-Agel (2020b), for a anti-clockwise rotating wake in an undisturbed shear layer with a positive vertical velocity gradient in the rotor area, it follows from the streamwise momentum equation that the momentum balance causes the wake to deflect to the left. Conversely, the difference in tip vortex strength between the upper and lower half of the wake will tend to deflect it to the right. These two opposing effects, which are not captured by the axisymmetric DWM wake models, likely explains why $\mathrm{LES_{UU}}$ predicts a greater wake deflection than the DWM models. Similarly, differences in

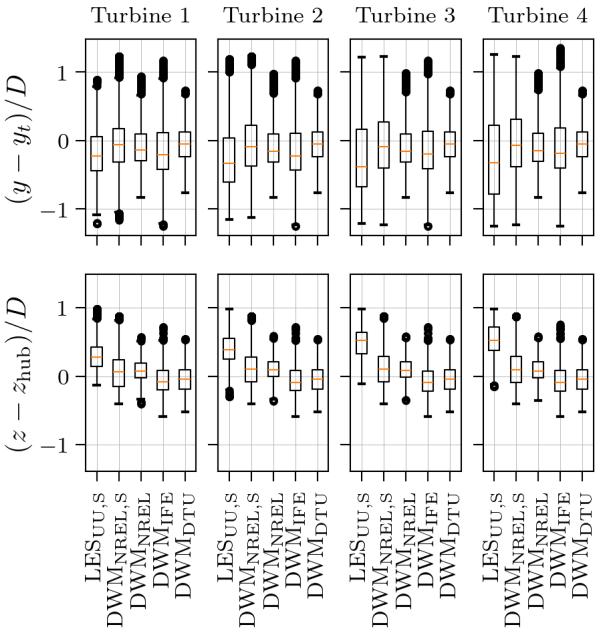

Figure 8. Box plots of horizontal (upper row) and vertical (lower row) wake centre positions at $x = 5D$ behind the turbines, for the aligned incoming wind case with high ambient turbulence ($\mathrm{TI_a}$ = 12 %).

tip vortex strength between the left and right sides of the wake, captured in the three-dimensional $\mathrm{LES_{UU}}$ flow, can drive the wake upward, explaining the larger upward wake deflections in $\mathrm{LES_{UU}}$ compared to DWM.

All models show grater horizontal meandering than vertical, and all show increased meandering at higher $\mathrm{TI_a}$. For turbine 1, the models agree well on the meandering level. However, $\mathrm{DWM_{IFE}}$ tends to produce slightly more meandering than the other DWM models. It matches LES more closely in the low ambient turbulence case but slightly overestimates meandering at high ambient turbulence. According to Keck et al. (2013), a lower wake transport velocity leads to increased levels of meandering, consistent with the higher meandering levels for $\mathrm{DWM_{IFE}}$ relative to $\mathrm{DWM_{DTU}}$. $\mathrm{DWM_{NREL}}$ and $\mathrm{DWM_{NREL,S}}$ show excellent agreement in median wake positions for all ambient turbulence cases, and in meandering levels for the low ambient turbulence case. However, at high ambient turbulence, $\mathrm{DWM_{NREL,S}}$ predicts a larger wake position spread than $\mathrm{DWM_{NREL}}$. This is expected as the SAMWICh algorithm becomes less accurate with increasing background turbulence, since the turbulence effectively acts as noise for the tracking algorithm.

For turbines 2–4, the wake position distributions diverge more between the models. While the wake of $\mathrm{LES_{UU}}$ shows a ~ 50 % increase in wake spread from turbine 1 to 2, the DWM models show no significant change. The wake meandering of $\mathrm{LES_{UU}}$ continues to increase from turbine 2 to 4. In DWM, however, all turbine wakes are subjected to the same ambient turbulence field, with no contribution from wake-added turbulence to meandering. Therefore, the meandering does not increase for downstream turbines. It is also worth noting that SAMWICh tracks the combined effect from all upstream wakes; for

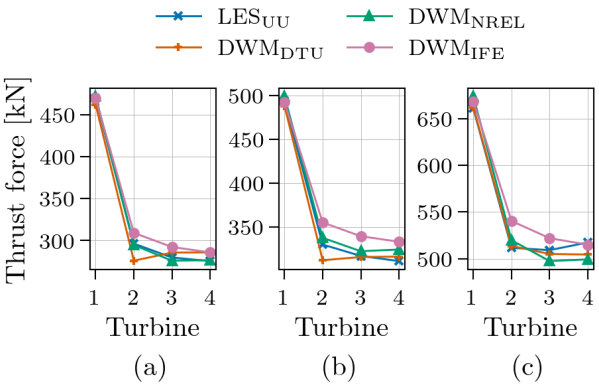

Figure 9. Mean thrust force for the aligned incoming wind case with (a) low (TI_a = 4.6 %), (b) medium (TI_a = 8.8 %), and (c) high (TI_a = 12 %) ambient turbulence.

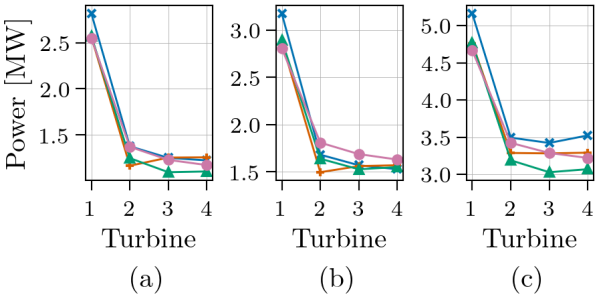

Figure 10. Mean power for the aligned incoming wind case with (a) low (TI_a = 4.6 %), (b) medium (TI_a = 8.8 %), and (c) high (TI_a = 12 %) ambient turbulence. For legend, see Fig. 9.

example at turbine 4 it identifies the sum of the wakes from turbine 1 to 4. Because the meandering of an isolated wake grows with downstream distance, the upstream turbine wakes, which have travelled farther, might contribute additional meandering to the combined wake tracked downstream of turbines 2–4 by SAMWICh. In fact, DWM$_{NREL,S}$ shows a slight increase in meandering along the row for both TI_a = 4.6 % and TI_a = 12 % that is not present in DWM$_{NREL}$, suggesting that tracking the combined wake can capture some growth in meandering. Therefore, some differences in the apparent wake meandering between LES$_{UU}$ and the DWM models may arise from the different wake-centre identification methods.

3.1.3 Power and thrust

Figures 9 and 10 show time-averaged thrust and aerodynamic power for the three levels of ambient turbulence investigated. While all models are in good agreement for the thrust of turbine 1, LES$_{UU}$ predicts about 10 % higher power than the DWM models for this turbine. As expected, all models show a significant drop in both thrust and power from turbine 1 to turbines

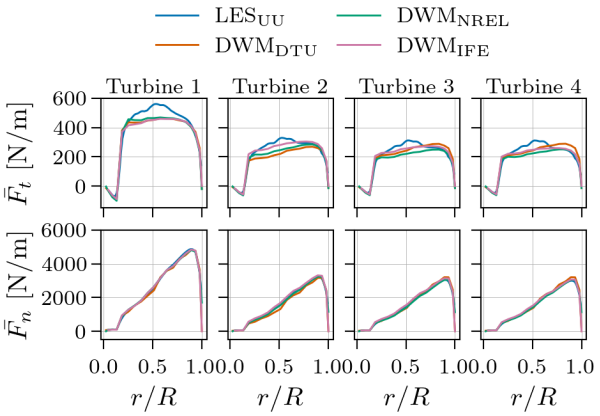

Figure 11. Time-averaged blade force as function of blade radius for the aligned incoming wind case with low ambient turbulence (TI_a = 4.6 %).

2–4 (which operate under waked conditions). For DWM$_{NREL}$, DWM$_{IFE}$, and LES$_{UU}$, thrust and power continue to decrease slightly from turbine 2 through 4 in the low and medium ambient turbulence cases. By contrast, DWM$_{DTU}$ shows a larger initial drop in thrust and power from turbine 1 to 2 compared to the two other DWM models. It then predicts an increase in these quantities from turbine 2 to turbines 3 and 4. A similar effect has been observed in full-scale measurements at the Lillgrund wind farm under comparable conditions (below-rated wind speeds, low ambient turbulence) but with more closely spaced turbines (see e.g., Madsen et al., 2016). At TI_a = 12 %, the drop from turbine 1 to 2 is smaller for all models, as expected with higher ambient turbulence due to faster wake recovery. For turbine 2 to 4, DWM$_{DTU}$ shows nearly constant thrust and power, instead of the increase seen at low and medium ambient turbulence. LES$_{UU}$, however, shows a slight increase in thrust and power from turbine 3 to 4 at TI_a = 12 %. This behaviour could be due to turbulence build-up along the turbine row, which accelerates wake recovery deeper into the farm.

3.1.4 Blade forces

Figure 11 shows the time-averaged tangential and normal force distributions along the radial positions of the blades for the low ambient turbulence case. The results are qualitatively similar for the higher ambient turbulence cases (Figs. A4 and A5 in Appendix A). Overall, the models are in good agreement. However, LES$_{UU}$ predicts higher tangential forces than the DWM models in the middle section of the blades, consistent with its higher power predictions in Fig. 10. Since turbine 1 experiences the same inflow in all models, the differences observed for that turbine must come from differences in the turbine aerodynamic models (ALM in LES$_{UU}$ and BEM variants in the DWM models; see Sect. 2.2.8 for details). Similar differences in the shape of the tangential force distribution between ALM and BEM have been reported in previous studies (Liu et al., 2022), though not as pronounced as observed here. The force-distribution plots further show that for the TI_a = 4.6 % and TI_a = 8.8 % cases, where DWM$_{DTU}$ predicts increased thrust and power for turbines 3 and 4 relative to turbine 2, both normal and tangential

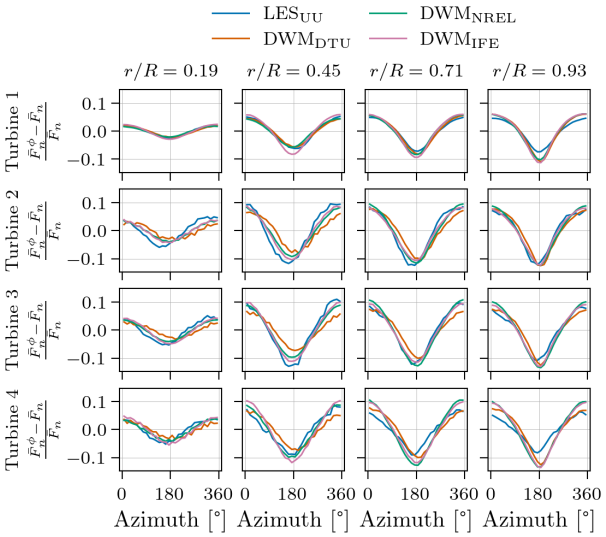

Figure 12. Relative difference between mean normal blade force per azimuthal bin $\bar{F}_n^\phi$ and total normal force $\bar{F}_n$, for the aligned incoming wind case with low ambient turbulence (TI_a = 4.6 %).

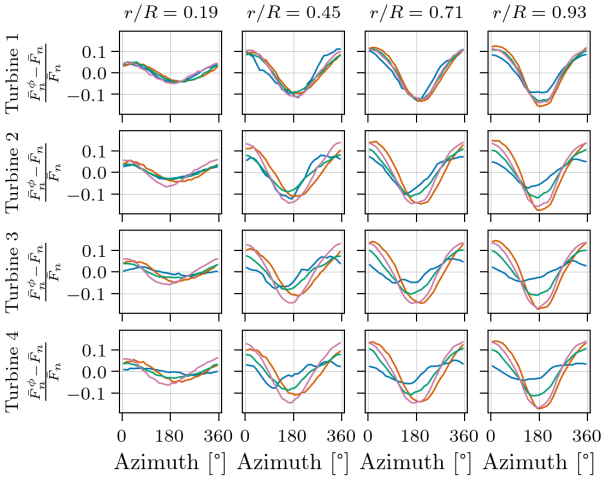

Figure 13. Relative difference between mean normal blade force per azimuthal bin $\bar{F}_n^\phi$ and total normal force $\bar{F}_n$, for the aligned incoming wind case with high ambient turbulence (TI_a = 12 %). For legend, see Fig. 12.

forces tend to be higher compared to the other models at the outer part of the blade ($r/R > 0.5$) for the two last turbines in the row. For the normal forces, which are nearly an order of magnitude larger than the tangential forces, the relative differences between the models are small.

Figures 12 and 13 show the azimuthal variation of the normal component of the blade force at four radial blade positions for the low and high ambient turbulence cases, respectively (the medium ambient turbulence case is given in Fig. A6 in Appendix A). The time-averaged normal force at each radial position, $\bar{F}_n$ (from Fig. 11), has been subtracted from the azimuthally varying force, and the result normalized by $\bar{F}_n$ to show only the relative force variation over a rotation. $\bar{F}_n^\phi$ is azimuthally binned by $\Delta\phi = 12^\circ$ using all blade rotations from the 45 min simulation. The maximum blade force occurs around $\phi = 0^\circ$, when the blade points upwards and experiences the highest wind speeds. Conversely, the minimum blade force occurs around $\phi = 180^\circ$. As noted in Sect. 2.1, the tower is not modelled, so any variation in wind speed experienced by the blades is solely due to wind shear and, for turbines 2–4, the influence of upstream wakes. In all models, the amplitude of force variation increases towards the blade tip, for every turbine.

For the low ambient turbulence case in Fig. 12, the models generally agree on the shape of the force variation. However, the phase of the $\mathrm{DWM_{DTU}}$'s force variation is slightly shifted to higher ϕ for turbines 2–4 compared to the other models. The force variation amplitudes also generally agree well between the models, however, $\mathrm{LES_{UU}}$ shows slightly smaller amplitudes than the DWM models at $r/R = 0.93$, even for turbine 1 where all models share the same inflow. As before, differences observed for this turbine arise from differences in the turbine aerodynamic models. In particular, the deviations at $r/R = 0.93$ is likely related to the tip corrections. The ALM in $\mathrm{LES_{UU}}$ uses a vortex-based tip-smearing correction, whereas BEM in the DWM models applies the Prandtl tip correction (see Sect. 2.2.8 for details).

For high ambient turbulence, Fig. 13, the model differences are more pronounced. For the turbines operating under waked conditions, $\mathrm{LES_{UU}}$ exhibits a phase shift to smaller ϕ (i.e., peaks occur at $\phi < 180^\circ$), whereas $\mathrm{DWM_{DTU}}$ again shows a slight shift to larger ϕ (peaks at $\phi > 180^\circ$). In $\mathrm{LES_{UU}}$, this shift is greatest for turbine 3 and 4: the maxima move from about 0° to 300°, and the minima from around 180° to 150°. As noted earlier (Fig. 8), the wakes shift slightly to the right when looking downstream (tonegative y), which shifts the regime of highest wind to the left. Equivalently, the region of lowest wind shifts to the right, to $\phi < 180^\circ$. As in the $\mathrm{TI_a}$ = 4.6 $\%$ case, $\mathrm{LES_{UU}}$ predicts smaller force variation amplitudes than the DWM models at the blade tip for turbine 1, supporting the conclusion that there are differences in the turbine aerodynamic models. For the turbines operating under waked conditions (2–4), the models show large deviations in amplitude. $\mathrm{LES_{UU}}$ yields smaller force variation amplitudes than the DWM models, with $\mathrm{DWM_{NREL}}$ coming closest. While the amplitudes of the force variations remain approximately constant for all turbines in $\mathrm{DWM_{DTU}}$ and $\mathrm{DWM_{IFE}}$, they decrease downstream along the turbine row for $\mathrm{LES_{UU}}$ and $\mathrm{DWM_{NREL}}$.

For turbines 2–4, differences in their incoming wind fields are the main source of the discrepancies in blade force variations between the models. The amplitudes of the force variations depend on the variation in velocity that the blades experience over a rotation. For instance, a vertical velocity profile with smaller variations over the rotor-swept area, as seen in $\mathrm{LES_{UU}}$ at $x_{t=3} = -D$ and $x_{t=4} = -D$ in Figs. 2 and 3, yields smaller force variations on the blades of turbine 3 and 4. Conversely, the higher velocity gradients in the $\mathrm{DWM_{DTU}}$ and $\mathrm{DWM_{IFE}}$ profiles result in larger force variation amplitudes.

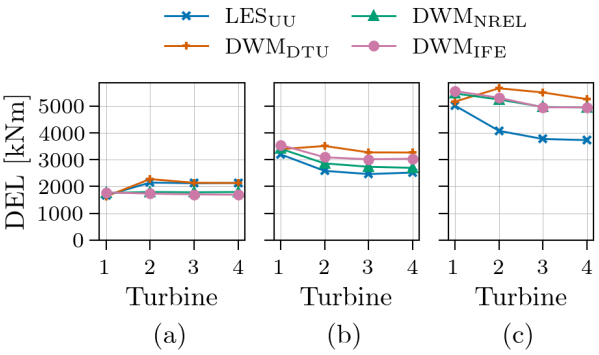

Figure 14. Fatigue of blade-root flapwise bending moment for the aligned incoming wind case with ambient turbulence of (a) TI_a = 4.6 %, (b) TI_a = 8.8 %, and (c) TI_a = 12 %.

3.1.5 Fatigue

Figure 14 shows 45 min damage-equivalent loads (DELs: see Sect. 2.1 for details) for the blade-root flapwise bending moment, using a Wöhler coefficient of 10 for the blades. For the low ambient turbulence case, Fig. 14 (a), LES$_{UU}$ shows a large increase in DEL from turbine 1 to 2, followed by a constant level further down the turbine row. DWM$_{DTU}$ agrees very well with LES$_{UU}$ in this case, except it gives a slightly higher DEL at turbine 2. By contrast, DWM$_{NREL}$ and DWM$_{IFE}$ do not capture this increase in DELs from turbine 1 to 2, but predict nearly the same DEL for all turbines.

Figure 14 also shows that blade-root flapwise bending moment DELs increase with ambient turbulence for all models. DWM$_{DTU}$ shows a similar trend from turbine 1 to 4 at all TI_a levels: an increase from turbine 1 to 2, and then a slight decrease for the turbines further downstream. The other models show a different development along the turbine row at higher TI_a. At TI_a = 8.8 % and TI_a = 12 %, LES$_{UU}$ estimates a substantial decrease (about 15–20 %) from turbine 1 to 2, followed by roughly constant levels from turbine 2 to 4. DWM$_{NREL}$ and DWM$_{IFE}$ show a similar trend along the turbine row, but at higher overall DEL levels.

To investigate these DEL differences, Fig. 15 presents the power spectral density (PSD) of the blade-root flapwise bending moment, shown as cumulative integrals. All models' spectra exhibit jumps at the $1P$ frequency and its harmonics, as well as in the low-frequency range below f_c. $1P$ corresponds to the frequency of one blade revolution, and the jumps in the cumulative integral correspond to peaks in the standard PSD. $f_c = U_\infty/(2D)$ is the meandering cut-off frequency, and loads associated with wake meandering are expected to appear below f_c (Larsen et al., 2008; Larsen and Lio, 2025). However, since turbine 1 experiences undisturbed inflow without (no upstream wake), its energy in the PSD below f_c represents a baseline without wake meandering energy. Surprisingly, DWM$_{DTU}$ is the only model consistently estimates a significant increase in energy below f_c when comparing turbine 1 to the turbines operating under waked conditions. LES$_{UU}$ does show some variation in energy below f_c, for example an increase from turbine 3 to 4 in the low ambient turbulence case. This change aligns with the increased meandering observed in Fig. 7, particularly in the lateral direction.

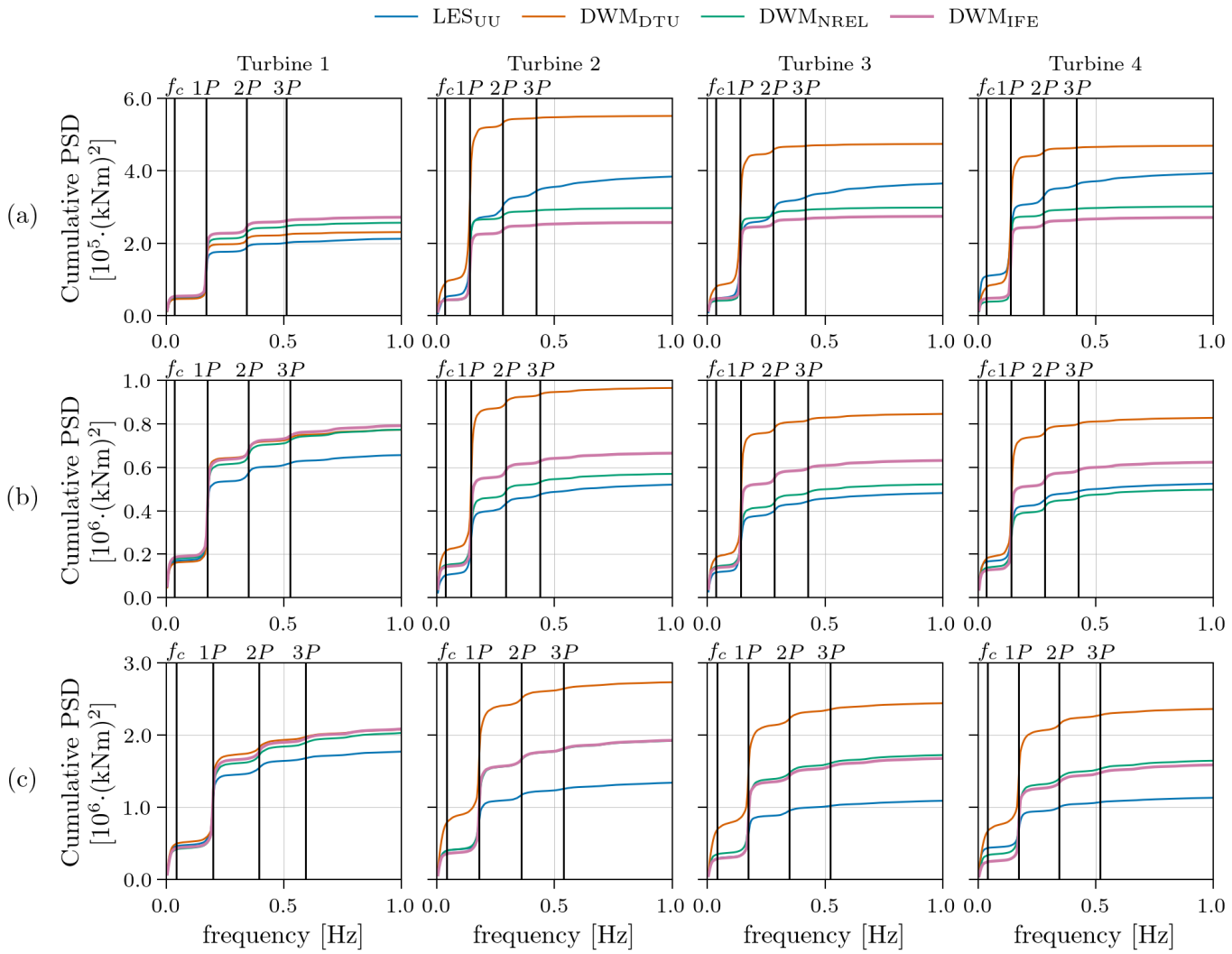

Figure 15. Energy spectra of blade-root flapwise bending moment for the aligned incoming wind case with ambient turbulence of (a) TI_a = 4.6 %, (b) TI_a = 8.8 %, and (c) TI_a = 12 %.

DWM$_{NREL}$ and DWM$_{IFE}$ show fairly good agreement with LES$_{UU}$ in terms of energy at the $1P$ frequency. For these models, the $1P$ energy levels scale with the amplitudes of the blade-force variations in Figs. 12–13: DWM$_{IFE}$ has the highest amplitudes and highest $1P$ energy, and LES$_{UU}$ the lowest. DWM$_{DTU}$, however, shows significantly higher $1P$ energy for the turbines operating under waked conditions (especially for turbine 2) compared to the other models, and the $1P$ energy does not scale with the blade-force variation amplitude. At frequencies above $1P$, LES$_{UU}$ shows higher energy levels in the waked turbines compared to turbine 1 for the low ambient turbulence case. Energy at the harmonics of $1P$ ($2P$, $3P$, $4P$, etc.) arises from asymmetric blade loading (i.e. deviations from purely sinusoidal force variation). In LES$_{UU}$, the instantaneous wakes

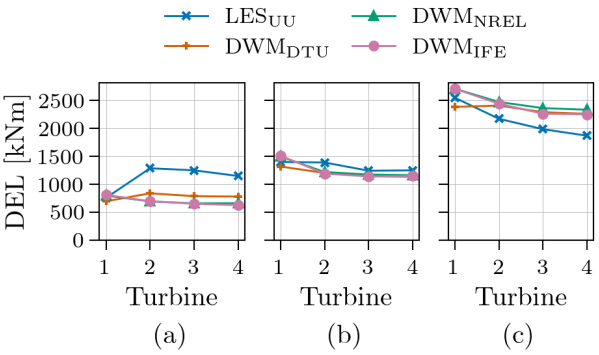

Figure 16. Fatigue of tower-top yaw moment for the aligned incoming wind case with ambient turbulence of (a) TI_a = 4.6 %, (b) TI_a = 8.8 %, and (c) TI_a = 12 %.

can be highly asymmetric and only approximately axisymmetric on average, so turbine 2–4 experience increased energy at these harmonic frequencies compared to turbine 1. In addition, wake-generated turbulence, which has a much smaller length scale than the ambient turbulence (Madsen et al., 2010), contributes to increased energy at higher frequencies for the turbines operating under waked conditions. None of the DWM models predict a notable increase in high-frequency energy for the waked turbines. The DWM models assume axisymmetric wakes, which do not directly cause asymmetric blade loading on the turbines operating under waked conditions, only indirectly via meandering. Somewhat unexpectedly, DWM$_{DTU}$'s wake-added turbulence model does not generate the increased high-frequency energy for the waked turbines as was observed in the LES$_{UU}$ results. At higher ambient turbulence, even LES$_{UU}$ shows no visible increase in high-frequency energy from turbine 1 to turbines 2–4. This is likely because the wake-added turbulence in these cases is negligible compared to the already high ambient turbulence.

Even though DWM$_{DTU}$ matches LES$_{UU}$ well in terms of DELs for the low ambient turbulence case, the underlying contributions in the PSD differ between the two models. In DWM$_{DTU}$, the DEL increase from turbine 1 to turbines 2–4 is mainly driven by higher energy at $1P$ and also below f_c at all ambient turbulence levels. For LES$_{UU}$, the DEL increase in the low ambient turbulence case comes from a combination of increased energy associated with $1P$ frequency and higher. For the higher ambient turbulence cases, the negligible wake-added turbulence levels and the decreasing energy at $1P$ frequency in LES$_{UU}$ cause DELs to reduce along the turbine row. For these cases, DWM$_{NREL}$ and DWM$_{IFE}$ follow the same trend and are closest to LES$_{UU}$.

Figures 16 and 17 show 45-min DELs for the tower-top yaw moment and tower-base fore-aft bending moment, respectively, using a Wöhler coefficient of 3 for the tower. For all cases, the models show good agreement on turbine 1's tower DELs. For the low ambient turbulence case, LES$_{UU}$ predicts considerably higher tower DELs than the DWM models for turbines 2–4. Among the DWM models, DWM$_{DTU}$ comes closest to LES$_{UU}$ and is the only one to reproduce a similar development in DELs along the turbine row. At higher ambient turbulence, LES$_{UU}$ and the DWM models are in closer agreement for the turbines operating

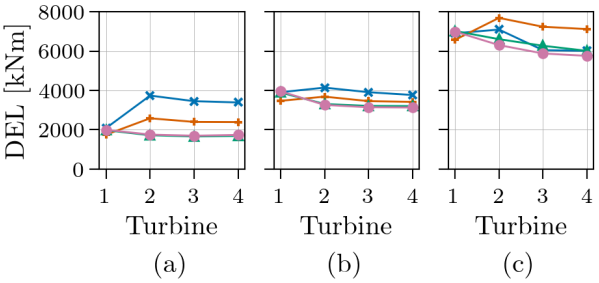

Figure 17. Fatigue of tower-base fore-aft bending moment for the aligned incoming wind case with ambient turbulence of (a) TI_a = 4.6 %, (b) TI_a = 8.8 %, and (c) TI_a = 12 %. For legend, see Fig. 16.

under waked conditions. Consistent with the blade load results, tower loads increase with ambient turbulence intensity. The cumulative PSD of the tower-base fore-aft bending moment in Fig. 18 shows jumps below f_c and at the $3P$ frequency for all models. LES_{UU} also exhibits energy at multiples of $3P$, visible as small jumps at $6P$. Energy below f_c contributes more significantly to tower loads than it did for blade loads shown in Fig. 15. Similar to the blade load results, DWM_{DTU} is the only model consistently predicting higher energy below f_c for turbines 2–4 compared to turbine 1. All models predict similar $3P$ energy for turbine 1. However, only LES_{UU} shows increased $3P$ and $6P$ energy for the downstream turbines relative to turbine 1. This is likely due to the asymmetric loading caused by the instantaneous LES wakes, as discussed earlier for the blade loads. These increases diminish with higher ambient turbulence, and by TI_a = 12 %, all models predict similar energy at $3P$ and above for every turbine. The tower-top yaw moment PSD in Fig. A7 in Appendix A shows qualitatively similar behaviour to the tower-base fore-aft moment.

3.2 Partially waked case

This section extends the analysis to a more complex inflow scenario by introducing a small misalignment between the mean wind direction and the turbine row. The resulting partial-wake configuration better reflects typical operational conditions in wind farms, where turbines are rarely aligned perfectly with the wind. The same ambient conditions as the medium ambient turbulence case in Sect. 3.1 are used, but with a 5° inflow angle offset relative to the turbine row and with no yaw misalignment of the turbines themselves. We evaluate model performance in terms of time-averaged flow fields, wake centre positions, power production, thrust forces, blade loads, and fatigue. The results allow us to further examine each model's ability to capture asymmetric flow and loading effects.

3.2.1 Mean velocity profiles

Figure 19 shows time-averaged velocity profiles at the axial positions $-1D$, $2.5D$, and $5D$ relative to each of the four turbines, for the partially waked case with ambient turbulence TI_a = 8.8 %. The upper row shows horizontal profiles at hub height and the lower row shows vertical profiles at the turbine's lateral centre. Horizontal dashed lines indicate the range of the turbine's

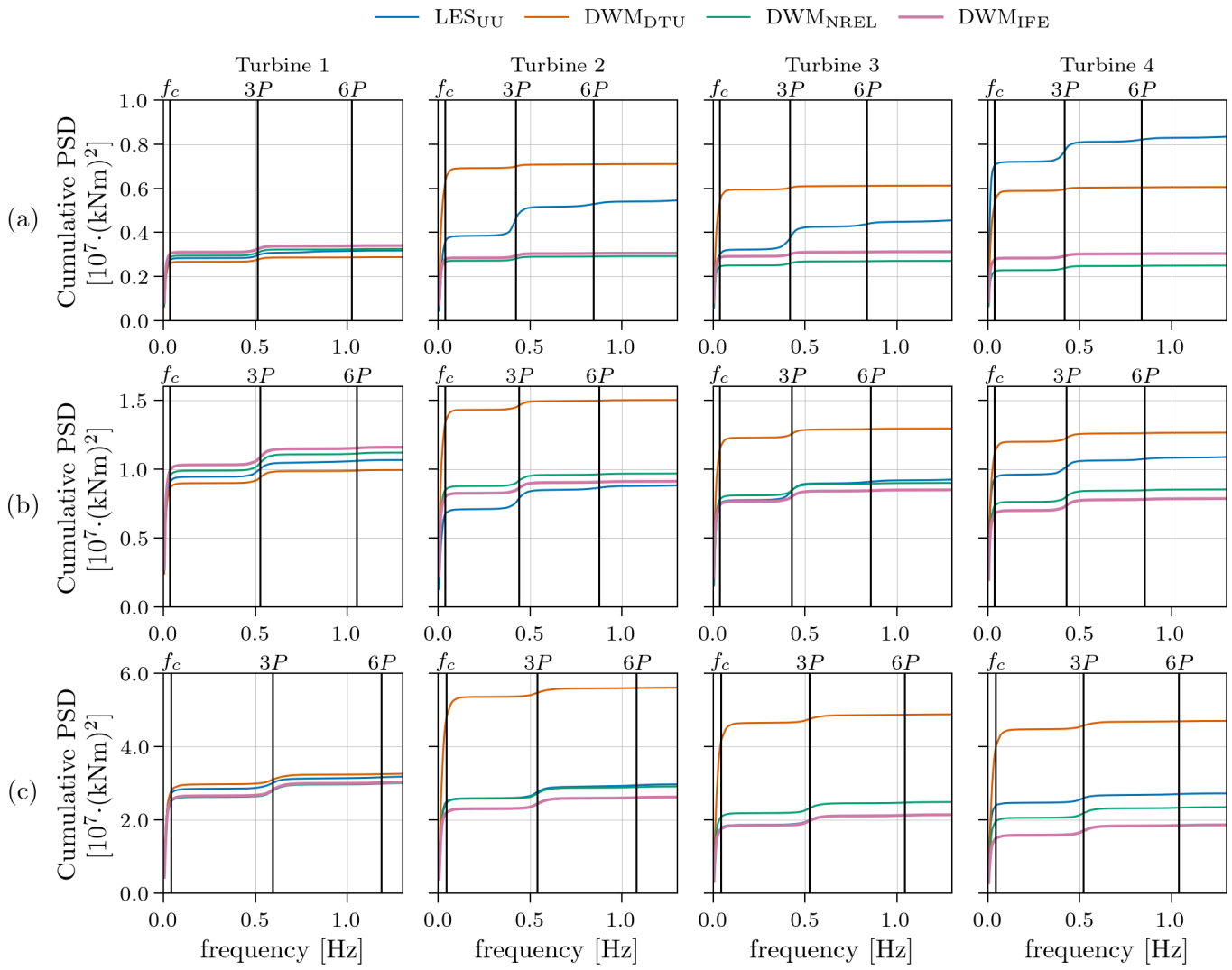

Figure 18. Energy spectra of tower-base fore-aft bending moment for the aligned incoming wind case with ambient turbulence of (a) TI_a = 4.6 %, (b) TI_a = 8.8 %, and (c) TI_a = 12 %.

rotor-swept area of the nearest upstream turbine, and horizontal dash-dot lines mark the lateral positions at which the corresponding vertical profiles are taken. Since the ambient conditions of the partially waked case match the fully waked case with medium ambient turbulence, the flow behind and the response of turbine 1 is similar: DWM$_{DTU}$ shows a distinct near-wake profile, whereas DWM$_{NREL}$ and LES$_{UU}$ show only traces of it. As in the fully waked case, DWM$_{IFE}$, and to a lesser degree DWM$_{NREL}$, tend to underpredict the centreline deficit. DWM$_{DTU}$, by contrast, slightly overpredicts the deficit in turbine 1's wake compared to LES$_{UU}$, but then gradually underpredicts it further down the turbine row. Do to the asymmetric inflow

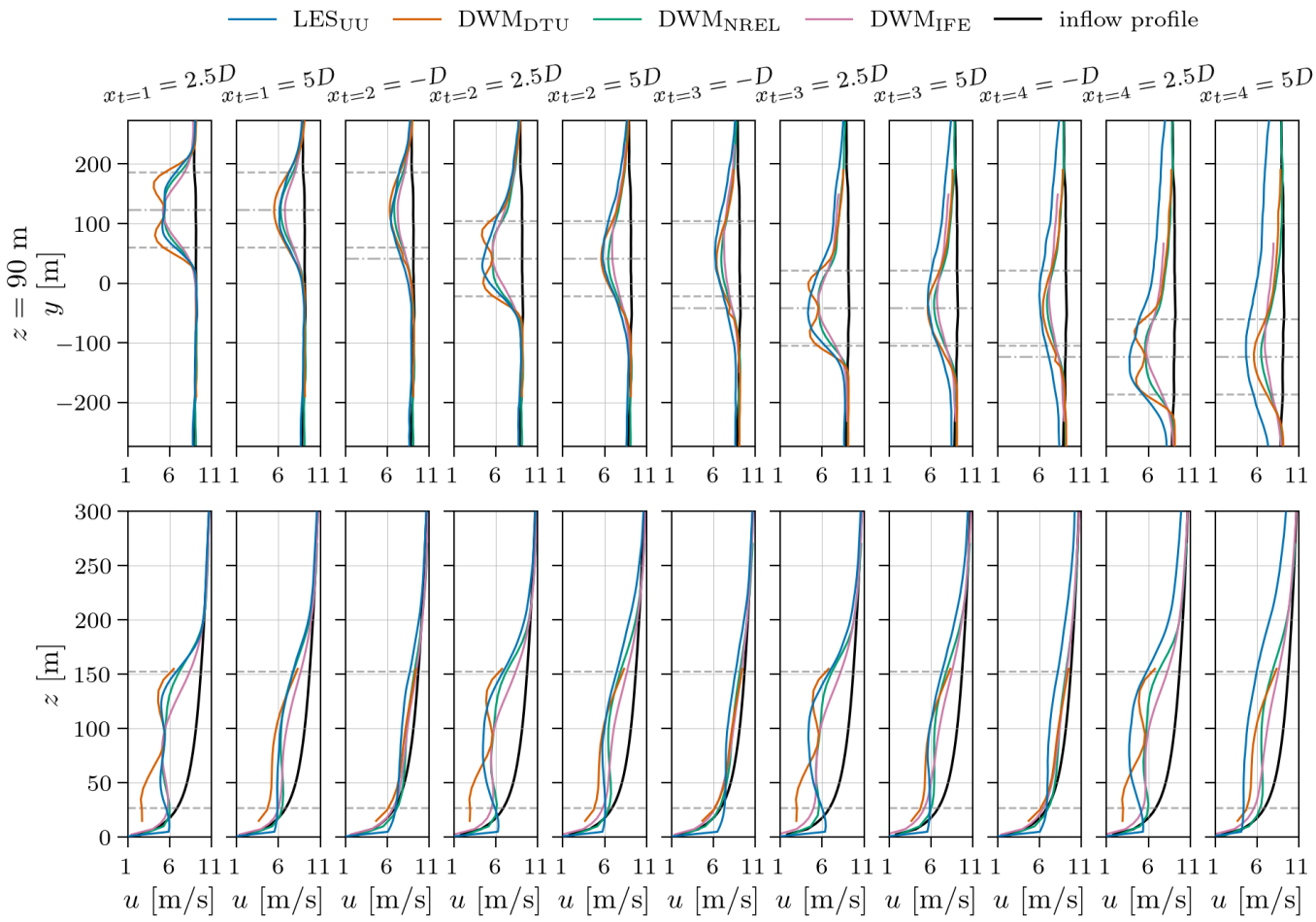

Figure 19. Time-averaged velocity profiles for the partially waked case (5° inflow angle) with medium ambient turbulence (TI_a = 8.8 %). Horizontal dashed lines indicate the rotor swept area of the closest upstream turbine, and horizontal dash-dot lines indicate at which lateral position the corresponding vertical profiles are plotted.

for turbines 2–4, all models predict that the wakes of these turbines spread more to the left side when looking downstream. However, as in the fully waked case, LES$_{UU}$ shows a greater increase in deficit outside and above the rotor span compared to the DWM models deeper into the turbine row.

Figure 20 shows profiles of velocity standard deviation σ_u for the partially waked case. As in the fully waked case with medium ambient turbulence, LES$_{UU}$ and DWM$_{DTU}$ show much higher σ_u levels than DWM$_{NREL}$ and DWM$_{IFE}$. DWM$_{DTU}$ matches LES$_{UU}$ particularly well in the shear-layer on the right side of the wake when looking downstream, whereas larger differences appear in the left-side shear-layer and in the vertical profile.

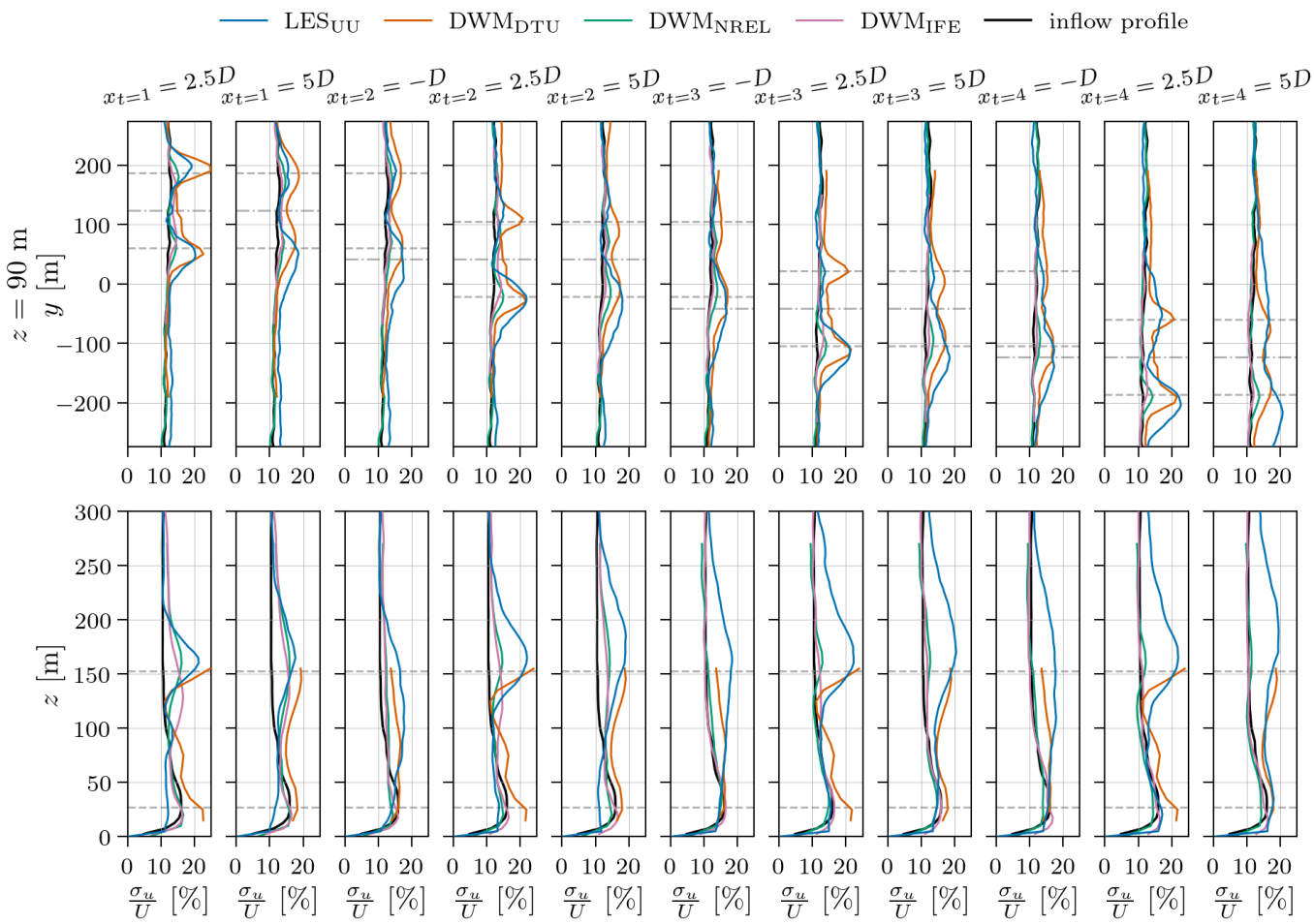

Figure 20. Profiles of velocity standard deviation for the partially waked case (5° inflow angle) with medium ambient turbulence (TI_a = 8.8 %). Horizontal dashed lines indicate the rotor swept area of the closest upstream turbine, and horizontal dash-dot lines indicate at which lateral position the corresponding vertical profiles are plotted.

3.2.2 Wake centre positions

Figure 21 shows box-and-whisker plots of the horizontal and vertical wake centre positions at $5D$ downstream of each turbine for the partially waked case. For LES$_{UU,S}$, the wake centre positions are tracked using the SAMWICh toolbox (Sect. 2.4), whereas for the DWM models the wake centre positions are taken directly from the meandering algorithm in the DWM simulation.

For turbine 1, all models predict that the median wake centre position stays approximately at the turbine position laterally ($y - y_t \approx 0$). For the DWM models, this holds for turbines 2–4 as well, whereas LES$_{UU,S}$ predicts the median wake centre

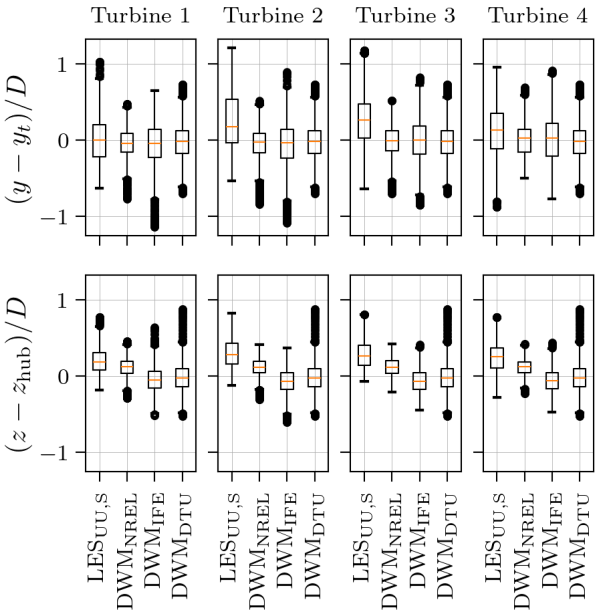

Figure 21. Box plots of horizontal (upper row) and vertical (lower row) wake centre positions at $x = 5D$ behind the turbines for the partially waked case (5° inflow angle) with medium ambient turbulence ($\mathrm{TI_a}$ = 8.8 %).

positions shifted slightly to the left when looking downstream ($y - y_t > 0$). In this skewed inflow setup, each turbine is offset to the left of the one behind it; for example, turbine 1 is located $0.65D$, $1.31D$, and $1.96D$ to the left of turbines 2, 3, and 4, respectively. Since SAMWICh tracks the combined wake from all the upstream turbines, the leftward shift in the $\mathrm{LES_{UU,S}}$ wake centre distributions may be influenced by the upstream wakes' position rather than a true deflection of the individual wakes. Alternatively, this asymmetry could be caused by the vertical shear in the inflow causing a horizontal wake deflection, as discussed in Sect. 3.1.2. However, that mechanism does not explain why only the wakes of turbines 2–4 show a leftward deflection and not the wake of turbine 1, nor why the deflection is in the opposite direction to what was seen in the aligned inflow case.

As in the aligned inflow cases (Sect. 3.1), $\mathrm{LES_{UU}}$ and to a lesser extent $\mathrm{DWM_{NREL}}$ predict that the wakes deflect upward above hub height because of the 5° rotor tilt. And also in agreement with the previous results, all models show more horizontal than vertical meandering. However, unlike the aligned case, $\mathrm{LES_{UU}}$ does not show a large increase in meandering levels further down the row under partial-wake conditions.

3.2.3 Power and thrust

Figure 22 shows time-averaged thrust force and power for each turbine in the partially waked case. As expected, turbine 1 exhibits similar thrust and power as the fully waked case with the same medium ambient turbulence conditions. However,

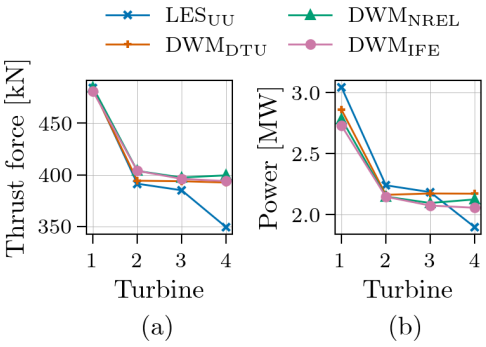

Figure 22. (a) Mean thrust force and (b) mean power for the partially waked case (5° inflow angle) with medium ambient turbulence (TI_a = 8.8 %).

small differences due appear because of variations in the incoming wind field at the two lateral positions of turbine 1 in the fully waked case (y =0) and in the partially waked case ($y \approx$123 m). As in the fully waked case, LES$_{UU}$ shows about 10 % higher power compared to the DWM models for turbine 1. For turbines 2–4, the DWM models are in good agreement, whereas LES$_{UU}$ shows a significant drop in both thrust and power between turbine 3 and 4. This drop comes from the deeper deficit in front of turbine 4 as a result of a much wider horizontal wake predicted by LES$_{UU}$, visible at $x_{t=4} = -D$ in Fig. 19.

3.2.4 Blade forces

The time-averaged tangential and normal force distributions along the blade span for the partially waked case (Fig. A8 in Appendix A) show qualitatively similar trends to the fully waked case, with good agreement among the DWM models, while LES$_{UU}$ shows higher tangential forces in the mid-span region of the blades. Figure 23 presents the azimuthal variation of the normal blade force at four radial positions along the blade for all four turbines in the partially waked case. For turbine 1, the models generally agree on the shape of the force variations, with some amplitude differences near the blade tip. However, larger deviations are seen among the models for turbines 2–4 under partially waked conditions. In LES$_{UU}$, the force minimum is shifted about 90° towards larger ϕ for turbines 2–4, meaning that the lowest force occurs when the blades point straight to the left. The lowest velocity in the incoming wind field is therefore towards the wake of the upstream turbine. For DWM$_{IFE}$, on the other hand, the minimum force is shifted only slightly towards larger ϕ. Because DWM$_{IFE}$ predicts a weaker wake deficit, the blades experience the lowest force when near the bottom of their rotation, where the velocity of the incoming flow is low due to shear. DWM$_{DTU}$ and DWM$_{NREL}$ predict a force minimum at about the same ϕ as LES$_{UU}$ for all radial positions along the blade. However, at the outer part of the blade, a second minimum appears at approximately the same ϕ as estimated by DWM$_{IFE}$. When a blade is pointing downward, its tip passes through a region where the DWM models predict significantly sharper vertical velocity gradients than LES$_{UU}$ (see Fig. 19). As a result, the DWM models predict a force minimum at $\phi \approx$180° on the outer blade sections, even under partially waked conditions.

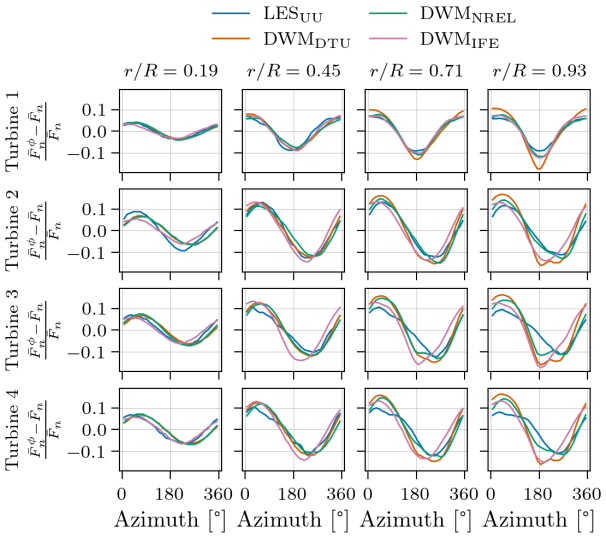

Figure 23. Relative difference between mean normal blade force per azimuthal bin $\bar{F}_n^\phi$ and total normal force $\bar{F}_n$ for the partially waked case (5° inflow angle) with medium ambient turbulence (TI_a = 8.8 %).

3.2.5 Fatigue

Figure 24 shows the 45-min DELs for (a) blade-root flapwise bending moment, (b) tower-top yaw moment, and (c) tower-base fore-aft bending moment, for the partially waked case. DWM$_{DTU}$ is the only DWM model to capture a similar development along the turbine row as LES$_{UU}$. However, it slightly overpredicts the blade DELs and underpredicts the tower DELs compared to LES$_{UU}$. DWM$_{DTU}$ and LES$_{UU}$ both estimate increasing DELs from turbine 1 to 2. In these models, the reduced loads due to decreased mean wind are compensated by increased turbulence downstream of turbine 1, modelled in DWM$_{DTU}$ by the wake-added turbulence model. By contrast, DWM$_{NREL}$ and DWM$_{IFE}$ lack a wake-added turbulence model, with the result that turbines 2–4 have lower DELs than turbine 1.

The PSDs of the loads presented in Fig. 25 show that DWM$_{DTU}$ predicts more energy below f_c for turbines 2–4 than the other models, as was also seen in the fully waked case. However, in the fully waked case LES$_{UU}$ showed no significant change in energy below f_c along the turbine row, whereas here LES$_{UU}$ does exhibit an increase in low-frequency energy from turbine 1 to the waked turbines for both the blade-root flapwise and tower-base fore-aft bending moments.

The blade-root flapwise bending moment spectra in Fig. 25 (a) show that the DWM models estimate more energy at the $1P$ frequency and its harmonics than the LES$_{UU}$ for all turbines, which is likely the main cause of the higher DELs estimated by the DWM models. As in the fully waked case, the levels of energy at the $1P$ frequency correspond well with the blade-force variation amplitudes seen in Fig. 23 for all models except DWM$_{DTU}$. Again, DWM$_{DTU}$ does not show a direct relationship between $1P$ energy and blade-force variation amplitude: it predicts a larger increase in $1P$ energy from turbine 1 to the waked turbines than the blade-force variation amplitude indicates.

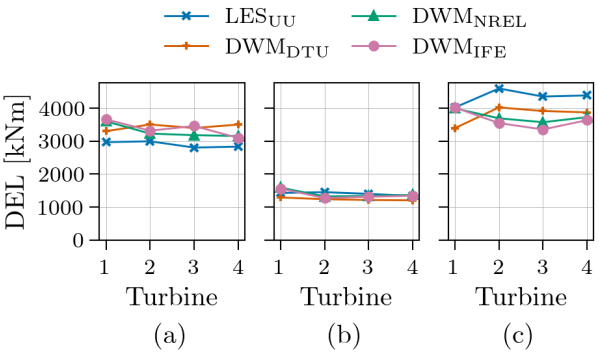

Figure 24. Fatigue of (a) blade-root flapwise bending moment, (b) tower-top yaw moment, and (c) tower-base fore-aft bending moment for the partially waked case (5° inflow angle) with medium ambient turbulence (TI_a = 8.8 %).

In the frequency spectra of tower-top yaw moments in Fig. 25 (b), LES_{UU} shows no significant change in energy below f_c between the turbines, while the small decrease in $3P$ energy along the turbine row coincides well with the change in DELs. DWM_{NREL} and DWM_{IFE} show a significant decrease in energy below f_c for the turbines operating under waked conditions, which, together with a decrease in energy at $3P$ frequency, reduce the tower-top yaw moment DELs. Finally, DWM_{DTU} shows nearly constant DELs as a result of increased energy below f_c and decreased energy at $3P$ frequency for the waked turbines compared to turbine 1.

For the tower-base fore-aft bending moment, DWM_{NREL} and DWM_{IFE} show DEL trends that correlate with the energy at $3P$ frequency, whereas for LES_{UU} and DWM_{DTU}, changes in energy below f_c dominate the DEL evolution along the turbine row.

4 Discussion

The comparative evaluation of the three DWM-based wake models against LES reveals generally good agreement in overall wake evolution and turbine performance trends, with notable discrepancies in specific wake features and load predictions.

4.1 Wake modelling

All three DWM models capture the qualitative shape and decay of the wake deficits along the turbine row, but there are systematic differences in deficit magnitude and shape when compared to LES. Immediately downstream of the first turbine, the DWM_{DTU} model produces a more pronounced near-wake profile than observed in the LES, whereas DWM_{NREL} tends to produce a deficit that is more developed towards a Gaussian profile. For the turbines operating under waked conditions, LES_{UU} already shows a Gaussian-like velocity profile at $x = 2.5D$. This is likely due to added turbulence in the turbine wakes, which increases the turbulence levels experienced by downstream turbines and enhances wake recovery through faster mixing.

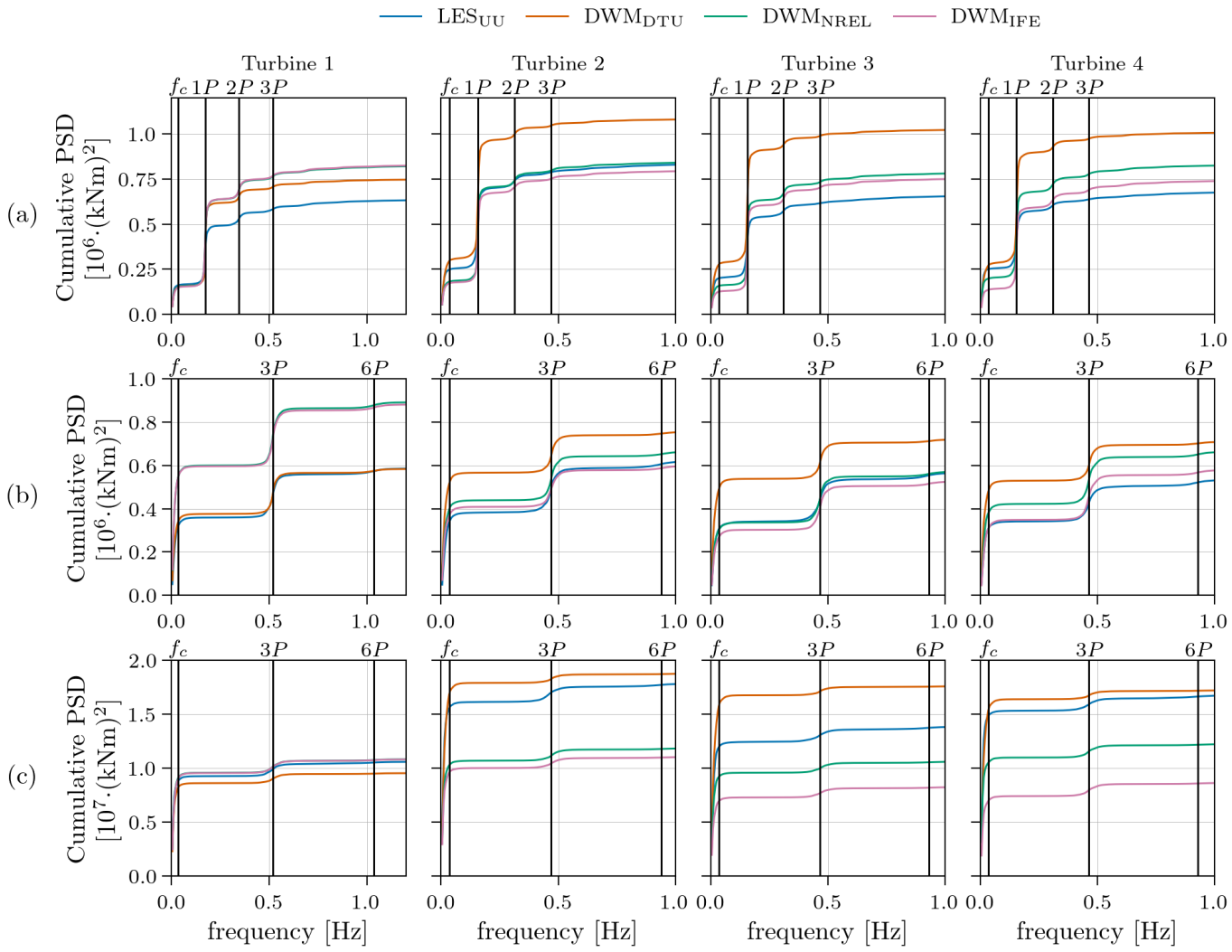

Figure 25. Energy spectra of (a) blade-root flapwise bending moment, (b) tower-top yaw moment, and (c) tower-base fore-aft bending moment for the partially waked case (5° inflow angle) with medium ambient turbulence (TI_a = 8.8 %).

Neither DWM$_{DTU}$ nor DWM$_{NREL}$ capture this increase in wake recovery rate between turbine 1 and the downstream turbines operating under waked conditions. Interestingly, DWM$_{IFE}$'s Gaussian profile therefore tend to outperform the other DWM models in the near-wake region of the waked turbines. Although DWM$_{DTU}$ includes a wake-added turbulence model, it is only applied in the aeroelastic solver and does not influence wake development. Consequently, increased wake recovery due to elevated downstream turbulence is not captured in the velocity field. The newly implemented wake-added turbulence model in DWM$_{NREL}$ couples wake-added turbulence with meandering (Branlard et al., 2024). Although it was not applied in this study,

it may improve agreement in future comparisons. Nonetheless, both $\mathrm{DWM_{DTU}}$ and $\mathrm{DWM_{NREL}}$ exhibit faster wake recovery at higher ambient turbulence, as expected.

In the far-wake regions for the aligned case (e.g., $x_{t=i} = 5D$, $x_{t=i+1} = -D$), $\mathrm{DWM_{DTU}}$ generally overestimates the centreline deficit slightly, while $\mathrm{DWM_{IFE}}$ slightly underestimates it. $\mathrm{DWM_{NREL}}$ falls in between and is often closest to $\mathrm{LES_{UU}}$ in these regions. However, for the partial wake case $\mathrm{DWM_{DTU}}$ appears to match $\mathrm{LES_{UU}}$ most closely. The $\mathrm{DWM_{DTU}}$ model uses a superposition method in which, under below-rated conditions, the velocity deficit at each point is taken as the largest deficit among all individual meandering wakes of upstream turbines. In contrast, $\mathrm{DWM_{NREL}}$ and $\mathrm{DWM_{IFE}}$ incorporate wake summation schemes in which all upstream wakes, calculated sequentially down the row, contribute to the total flow field to varying extents. While $\mathrm{DWM_{NREL}}$ does not capture the evolution of the flow field along the turbine row significantly better than $\mathrm{DWM_{DTU}}$, $\mathrm{DWM_{IFE}}$ shows improved accuracy in the wake periphery, where the $\mathrm{LES_{UU}}$ deficit build-up is substantial. The accumulation of turbulence intensity along the turbine row in the $\mathrm{DWM_{IFE}}$ model, which affects its eddy-viscosity closure, may also contribute to the differences observed relative to the other DWM models. However, $\mathrm{DWM_{IFE}}$'s performance degrades at higher ambient turbulence, suggesting that the term in its eddy viscosity model related to ambient wind shear scaling with turbulence intensity should be calibrated.

Vertical velocity profiles play a critical role in load predictions as they affect the azimuthal variation of the inflow felt by turbine blades, directly influencing blade $1P$ loading. Rotor tilt induces an upward wake deflection, which is captured by $\mathrm{LES_{UU}}$ and by $\mathrm{DWM_{NREL}}$ (the only model that incorporates tilt), but not by $\mathrm{DWM_{DTU}}$ or $\mathrm{DWM_{IFE}}$. Notably, $\mathrm{LES_{UU}}$ predicts even greater upward deflections than $\mathrm{DWM_{NREL}}$. This deflection increases with downstream distance and occurs even in the low-turbulence case without any rotor tilt. Horizontal deflection is also observed in the $\mathrm{LES_{UU}}$ results. This suggests that wake rotation and tip vortex effects, which are not accounted for in current DWM formulations, cause additional deflections. The curled-wake extension to $\mathrm{DWM_{NREL}}$ (Branlard et al., 2023), which was not used in the present simulations, could potentially help reduce these discrepancies.

The box plots of wake centre positions show that the predicted meandering levels for the first turbine in the row agree well among all DWM models and $\mathrm{LES_{UU}}$. Wake meandering is consistently stronger in the horizontal direction than the vertical across all models, consistent with the fact that large-scale vertical turbulence energy is lower than large-scale lateral turbulence energy for conventional flat terrain conditions. However, the downstream growth of meandering amplitude is underrepresented: while $\mathrm{LES_{UU}}$ shows a $50\ \%$ increase from turbine 1 to 2 (with continued growth beyond), the DWM models maintain nearly constant meandering levels. This discrepancy may result from the models' reliance on the same ambient turbulence field for all wakes, without accounting for the additional turbulence from upstream wakes, which leads to underprediction of wake spreading in deep turbine arrays. Hanssen-Bauer et al. (2023) suggest that this could be addressed by coupling the wake-added turbulence model with the meandering routine, so that both ambient and wake-added turbulence contribute to wake motion. In fact, the new wake-added turbulence model in $\mathrm{DWM_{NREL}}$ (Branlard et al., 2024) implements this approach. However, if wake-added turbulence does significantly contribute to wake meandering, it is in conflict with the traditional DWM assumption that meandering is driven only by large-scale turbulence while wake-added turbulence captures smaller scales. Nevertheless, important future work is to check this assumption by testing the new $\mathrm{DWM_{NREL}}$ wake-added turbulence model.

As shown in the σ_u profiles (Figs. 4–6 and 20), the wake-added turbulence model in $\mathrm{DWM_{DTU}}$ clearly improves its turbulence predictions. $\mathrm{DWM_{NREL}}$ and $\mathrm{DWM_{IFE}}$, lacking such a scheme, significantly underpredict σ_u in the turbine wakes across all cases. The influence of wake turbulence on the flow field is evident in snapshots of instantaneous velocity profiles. In the low ambient turbulence case in Fig. A1, $\mathrm{DWM_{NREL}}$ and $\mathrm{DWM_{IFE}}$ show relatively smooth wake profiles, whereas $\mathrm{LES_{UU}}$ and $\mathrm{DWM_{DTU}}$ produce more turbulent profiles. In the high ambient turbulence case shown in Fig. A2 the wakes do not dominate the flow field as much due to the already high background turbulence, and differences between the models are less pronounced.

Even with a wake-added turbulence model, $\mathrm{DWM_{DTU}}$ still shows discrepancies relative to $\mathrm{LES_{UU}}$. These may partly stem from differences in wake shape that influence the added turbulence via the velocity gradient input. Furthermore, $\mathrm{DWM_{DTU}}$ clearly lacks a model for turbulence build-up along the turbine row, especially evident in the low ambient turbulence case. Here $\mathrm{LES_{UU}}$ shows increasing σ_u along the row even as the mean deficit and velocity gradients decrease, which contradicts the wake-added turbulence formulation in Eq. 7. A possible reformulation of the current wake-added turbulence approach could be to treat Eq. 7 as a source term (which it is) and then combine it with an accumulation term and a decay term. The DWM modelling improvements by Keck et al. (2015) should also be considered as they account for the impact of ambient vertical wind shear on eddy viscosity and model the build-up of wake-added turbulence. Comparisons with ALM simulations show that including these improvements can reduce turbulence-intensity deviations by up to 40 % by the eighth turbine in a row (Keck et al., 2015).

4.2 Power and thrust predictions

Despite differences in flow details, all three DWM-based models reproduce the general trends in time-averaged turbine power and thrust observed in the LES benchmark, staying within 5–10 % of the LES results. Surprisingly, while the DWM models show good agreement in power prediction for turbine 1 where the inflow is identical for all models, $\mathrm{LES_{UU}}$ consistently predicts about 10 % higher power output. This discrepancy arises because $\mathrm{LES_{UU}}$ predicts higher tangential forces in the middle sections of the blades compared to the DWM models, likely due to differences in the aeroelastic solver. If this turbine-model discrepancy is consistent across all wind speeds, its impact can be adjusted by normalizing all turbine powers by the power of turbine 1, as shown in Fig. 26 (see Appendix B for further discussion of this approach's validity). With this normalization, $\mathrm{LES_{UU}}$'s power output generally aligns well with $\mathrm{DWM_{NREL}}$ for all turbines, while $\mathrm{DWM_{DTU}}$ and especially $\mathrm{DWM_{IFE}}$ typically overestimate the power for turbines 2–4. The exception is the partially waked case with a 5° inflow angle relative to the turbine row, which reveals the consequence of the DWM models failing to capture the significant velocity-deficit build-up outside the rotor span. In $\mathrm{LES_{UU}}$, this build-up causes a drop in power from turbine 3 to turbine 4 that is not captured by the DWM models. For turbine 4, $\mathrm{LES_{UU}}$ estimates the power to be 17–18 % lower than in the DWM models. This highlights the importance of accurately predicting wake spreading, particularly under real-world conditions where perfect alignment is rare. Failing to capture wake spreading can lead to a non-negligible overestimation of a wind farm's annual energy production. In this regard, the momentum-conserving superposition method applied in $\mathrm{DWM_{IFE}}$ is a promising approach, as it produces greater wake spreading and a more accurate increase in the off-rotor-span deficit, particularly in the low ambient turbulence case. However, the generally poor performance of this DWM implementation in estimating wake-deficit strength

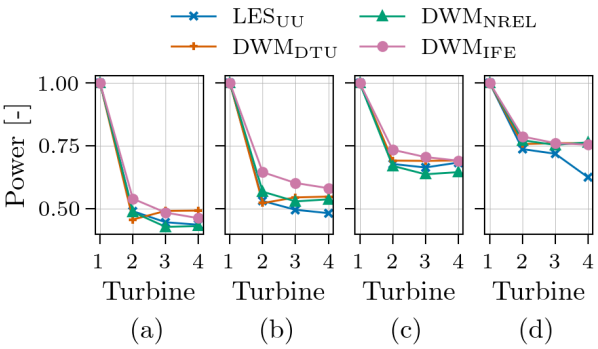

Figure 26. Mean power for the aligned incoming wind case with (a) low (TI_a = 4.6 %), (b) medium (TI_a = 8.8 %), (c) high (TI_a = 12 %) ambient turbulence, and (d) for the partially waked case (5° inflow angle) with medium ambient turbulence (TI_a = 8.8 %). For each model, the power outputs are normalized by the power of turbine 1.

for the medium and high ambient turbulence cases, prevents us from seeing the full potential of the momentum-conserving summation method in the partially waked scenario.

4.3 Fatigue-load predictions

Fatigue-load predictions represent the area of greatest divergence between the DWM and LES results, underscoring the challenges of modelling wake-induced unsteady inflow conditions and their structural consequences. While all three DWM models are able to reproduce the general trends in time-averaged loads (e.g., mean blade forces and mean thrust), their predictions of DELs vary substantially. The deviations are largest for the turbines operating under waked conditions, though differences are also evident for turbine 1, which likely originate from differences in the aeroelastic solvers. As with power, the influence of the aeroelastic solver can be limited by normalizing all turbine DELs by the DEL of turbine 1 (see Appendix B for a discussion of this approach's validity). The resulting normalized DELs for the blade-root flapwise bending moment and the tower-base fore-aft bending moment are shown in Figs. 27 and 28, respectively. Even though the normalization reduces the spread between the models slightly, the overall picture is the same. For the low ambient turbulence case, the DWM models tend to estimate lower blade loads and especially lower tower loads for the waked turbines compared to LES. For this case, DWM$_{DTU}$ is closest to LES$_{UU}$ in terms of DEL magnitude and its development along the turbine row. For higher ambient turbulence, the deviations between DWM and LES$_{UU}$ are smaller. The DWM models predict a larger increase in DELs with rising ambient turbulence compared to LES$_{UU}$. Consequently, in the high ambient turbulence case the DWM models, and especially DWM$_{DTU}$, predict higher DELs than LES$_{UU}$, particularly for blade loads.

Spectral analysis reveals that all DWM models tend to overestimate the energy content at the $1P$ frequency for the blade loads. This is related to higher azimuthal blade-force variations predicted by the DWM models, which is a direct consequence of the shapes of their predicted wake velocity profiles. However, for some models, especially DWM$_{DTU}$, the azimuthal blade-

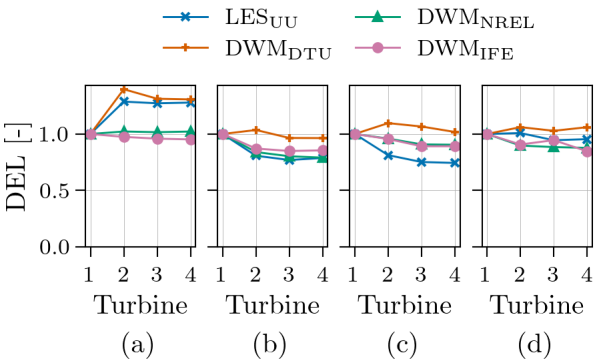

Figure 27. Fatigue of blade-root flapwise bending moment for the aligned incoming wind case with ambient turbulence of (a) TI_a = 4.6 %, (b) TI_a = 8.8 %, (c) TI_a = 12 %, and (d) for the partially waked case (5° inflow angle) with medium ambient turbulence (TI_a = 8.8 %). For each model, the DELs are normalized by the DEL of turbine 1.

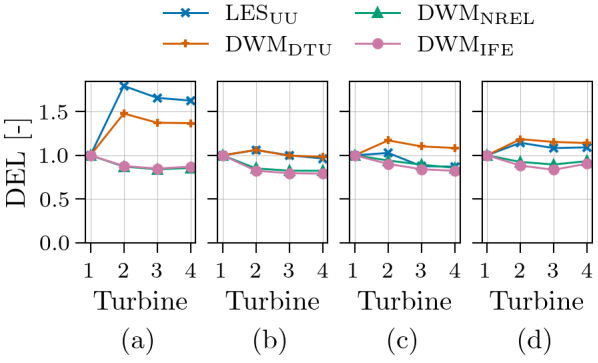

Figure 28. Fatigue of tower-base fore-aft bending moment for the aligned incoming wind case with ambient turbulence of (a) TI_a = 4.6 %, (b) TI_a = 8.8 %, (c) TI_a = 12 %, and (d) for the partially waked case (5° inflow angle) with medium ambient turbulence (TI_a = 8.8 %). For each model, the DELs are normalized by the DEL of turbine 1.

force variations seen in Figs. 12–13 and 23 do not scale with the energy at $1P$ frequency as expected. As explained in Hanssen-Bauer et al. (2023), this mismatch likely comes from a wake meandering effect. When an upstream wake meanders, it moves normal to the wind direction. This causes additional velocity gradients when a wake only partially covers a downstream turbines' rotor area. These partially waked conditions, caused by wake meandering, last for several blade rotations since the meandering motion is slower than the blade rotation ($f_c < 1P$). The effect is to a large extent not visible in the blade-force variation plots, because the forces are averaged in each azimuthal bin over the entire simulation. However, wake centre position plots show that DWM$_{DTU}$ does not predict higher meandering levels than the other models. Still, the load spectra for DWM$_{DTU}$ clearly show a significant increase in energy at low frequencies (associated with meandering) for the waked turbines relative

to turbine 1. This behaviour is not seen in the other models and suggests that in $\mathrm{DWM_{DTU}}$, meandering affects the loads more strongly than in the other models, possibly because $\mathrm{DWM_{DTU}}$ produces more distinct deficits with sharper radial gradients.

Consistent with findings for above-rated conditions by Hanssen-Bauer et al. (2023), we find that all DWM models tend to underestimate fatigue loading on downstream turbines, especially on the tower, if important turbulence-generation mechanisms are neglected. In the present below-rated cases, the $\mathrm{DWM_{DTU}}$ model with its wake-added turbulence model is the only DWM implementation that roughly captures the increased fatigue damage on the turbines exposed to upstream wakes relative to turbine 1 in the low ambient turbulence case. However, the magnitude of the increase in tower loads remains underpredicted. For higher ambient turbulence, the trend is less clear. For blade loads, $\mathrm{LES_{UU}}$ shows a decrease in DELs along the turbine row, whereas $\mathrm{DWM_{DTU}}$ still predicts an increase from turbine 1 to 2. This inconsistency appears to stem from different mechanisms causing the increased DELs in $\mathrm{DWM_{DTU}}$ versus $\mathrm{LES_{UU}}$ for the waked turbines. In $\mathrm{LES_{UU}}$, the high-frequency content of the load spectra is elevated, likely due to the higher small-scale turbulence in the wake. This effect is most pronounced in the low ambient turbulence case, since the relative increase in small-scale turbulence is greatest. $\mathrm{DWM_{DTU}}$, by contrast, seems to affect the loads more indirectly via wake meandering, as described in the previous paragraph. Wake-added turbulence could also play a role, as it might cause the meandering wakes with enhanced turbulence to have a greater effect on loads when they move in and out of the rotor-swept area. At higher ambient turbulence levels, the wake-added turbulence appears to play a smaller role in the fatigue-loading development along the turbine row in $\mathrm{LES_{UU}}$, while for $\mathrm{DWM_{DTU}}$ the enhanced meandering effect on loading continues to dominate.

Another important factor explaining the divergence between the DWM and LES fatigue results is the fact that the DWM models assume axisymmetric wakes that meander, whereas the instantaneous LES wakes can be highly asymmetric and only approximately axisymmetric on average.This difference is clearly illustrated by the snapshots of instantaneous velocity profiles for the low ambient turbulence case in Figs. A1. While for the DWM models the shapes of the instantaneous wake deficits can be recognised from the time-averaged ones in figure 1 for all turbines in the row, the LES wakes differ much more in shape. This asymmetry in the $\mathrm{LES_{UU}}$ flow is an important driver of loads, especially in the low ambient turbulence case, and appears as energy at higher harmonics of the blade rotational frequency, i.e. $2P$, $3P$, etc., for blade loads and $3P$, $6P$, etc. for tower loads. This phenomenon contributes to the DWM models' underprediction of loads. It aligns with the findings of Bernard et al. (2024), who investigated loads on a turbine under low-turbulence offshore conditions. Also here the traditional DWM models with axisymmetric wake deficits failed to capture the increased higher-harmonic content in the tower-top load spectra under waked conditions compared to free-inflow conditions. However, when a wake-distortion component was added to produce a non-axisymmetric wake in the DWM model, it showed better agreement with the measured load spectra and DELs.

An interesting observation is that $\mathrm{LES_{UU}}$ showed no significant change in energy below f_c for the fully waked case, but estimates increased energy below f_c from turbine 1 to turbines 2–4 in the partially waked case. This was seen for the blade-root flapwise bending moment and tower-base fore-aft bending moment, but not for the tower-top yaw moment. For turbines 2–4 in the partially waked conditions, the upstream neighbours are not directly ahead but offset laterally. As a result, lateral meandering relatively often moves the wake entirely away from the downstream turbine. This causes large fluctuations in blade-root and tower fore-aft moment on the meandering time-scale ($f < f_c$).

Overall, all DWM models struggle to capture the full range and correct intensity of wake-driven loading observed in LES. A better representation of turbulence evolution and its interaction with wake dynamics is crucial for improving fatigue-load predictions in DWM frameworks.

4.4 Weaknesses of the present study

While the comparative analysis provides valuable insights into the performance of DWM-based wake models, several limitations of the present study must be acknowledged.

First, all simulations were conducted at a single below-rated wind speed with the turbines operating at fixed RPM and pitch. This constrains the generalisability of the findings to other operational regimes, particularly near rated or cut-out wind speeds, where aerodynamic and control responses differ significantly. At higher wind speeds, turbine control strategies such as blade pitch and generator torque regulation may alter wake characteristics and structural responses in ways not captured in this study.

Second, the inflow conditions in both the LES and DWM simulations assume a neutral atmospheric boundary layer over homogeneous terrain, without thermal stratification. In reality, wind farms operate under more complex atmospheric conditions, including stable and unstable stratification, wind veer, and heterogeneous surface roughness. These factors influence turbulence intensity, wake deflection, and recovery, and may lead to larger discrepancies between engineering-fidelity models and field measurements.

Third, the modelled wind farm layout consists of a single row of four identical turbines with uniform spacing. While this configuration provides a controlled environment for model comparison, it lacks the complexity of real-world wind farms, where turbines are arranged in staggered rows or irregular layouts and are subject to multi-directional wake interactions. Moreover, the only non-aligned inflow condition tested involved a modest 5° offset, which is small relative to real-world offsets caused by wind-direction variability or wake-steering control strategies. Larger inflow angles, including turbine yaw misalignments, could lead to more complex wake dynamics that challenge current DWM formulations.

Fourth, the simulation durations were finite, so some load and flow statistics may be affected by sampling limitations (Liew and Larsen, 2022).

Fifth, validation against field measurements was not part of this study. While high-fidelity LES-ALM provides a physically consistent, high-resolution reference, these simulations do not necessarily reflect one-to-one full-scale measurements (Asmuth et al., 2022; Sood et al., 2022). The actuator-line method used in the LES model – though widely accepted as a high-fidelity approach – introduces its own approximations. The method represents blades as line forces rather than resolving blade-resolved flow features, which limits its accuracy in modelling near-wake vorticity, dynamic stall, and fine-scale unsteadiness. The lack of an elastic turbine model also means that structural Eigenmodes are not captured, which is particularly important for tower dynamics. Comparing model predictions against full-scale SCADA, lidar, and strain data would further strengthen the conclusions and reveal model limitations under real operational conditions.

Finally, the present comparison evaluates each DWM framework as a complete modelling system. Because several sub-models (e.g., wake-deficit formulations, wake-summation methods, meandering methods, and turbulence treatments) differ between implementations, differences in results cannot be attributed to any single modelling choice. As a consequence, some

interpretations of the causes behind model discrepancies remain qualitative. The present intercomparison reflects the combined effects of multiple sub-model differences. A more rigorous assessment would require controlled sensitivity studies where individual sub-models are varied or exchanged within a single framework to isolate their influence.

Future work should address these limitations by considering a broader range of operating conditions, including variable atmospheric stability and wind shear, and by evaluating model performance in more complex wind farm layouts. In addition, controlled sensitivity studies should be carried out to further disentangle the contributions of each modelling choice. Furthermore, improved turbulence modelling – both related to wake-added turbulence in individual wakes and turbulence development across a wind farm related to turbulence build-up and increased meandering levels – remains a key area for development in DWM frameworks. Asymmetries in turbine wakes, both in the instantaneous wake deficit and in a time-averaged sense due to wake deflections, also appear to be important drivers to fatigue damage that are not captured by current DWM models. Ultimately, continued benchmarking against both LES and high-quality field data is essential to advance the reliability of engineering-fidelity wake models for design and certification.

5 Conclusions

This study presents a comprehensive comparison of three DWM-based wake models (the DTU, IFE, and NREL implementations) against high-fidelity LES for a row of four wind turbines operating under below-rated wind conditions. The main findings indicate that all three engineering-fidelity models capture the general wake evolution and turbine performance with reasonable accuracy in terms of mean values. Specifically, the time-averaged turbine thrust force and aerodynamic power outputs from the DWM models generally align with the LES benchmarks (often within 5-10 $\%$), suggesting that the DWM framework is broadly reliable for estimating wind farm energy yield at below-rated wind speeds across various ambient turbulence intensities.

However, the DWM models still exhibit limitations in capturing the wake shape, unsteady wake dynamics, and cumulative downstream effects observed in LES, and each implementation show distinct strengths and weaknesses. Accurate modelling of far-wake shape is particularly important, as it influences both power output and structural loads on downstream turbines. For instance, the pronounced deficit build-up observed in the peripheral regions of the LES wake may significantly affect power estimates under partially waked conditions. In this regard, the IFE model's wake superposition approach and treatment of turbulence build-up via an eddy viscosity formulation appear to outperform the other models under low ambient turbulence conditions. At higher ambient turbulence levels, however, the benefit of these improvements is veiled by the IFE model's underprediction of wake-deficit strength. A more extensive calibration of the IFE model may therefore be necessary to enhance its performance under such conditions. In contrast, the DTU and NREL implementations with different wake summation models produce weaker wake expansion and less variation in incoming velocity among turbines 2–4, yet show better agreement with LES in terms of wake deficit strength and resulting power predictions for turbines operating under fully waked conditions. The NREL model also captures the upward wake deflection for turbines with rotor tilt, although not to the same extent as observed in LES.

Of critical concern are the substantial discrepancies in fatigue-load predictions between the DWM models and LES. Under low ambient turbulence conditions, all DWM implementations tend to underpredict fatigue damage on downstream turbines (especially in tower loads), whereas under high ambient turbulence they tend to overpredict fatigue loads. However, the DTU implementation, which includes a wake-added turbulence model, is generally the closest to LES in predicted fatigue load levels and best captures the load variations along the turbine row. These findings highlight the importance of accurately representing the increased turbulence in turbine wakes – both spatial variation and spectral content – as well as the downstream progression of turbulence and wake meandering across the wind farm. The current study also confirms previous findings that DWM's underprediction of fatigue damage at low ambient turbulence is partly due to the assumption of an axisymmetric wake deficit, which prevents the model from capturing important asymmetric load effects on downstream turbines.

While DWM models strike a favourable balance between accuracy and computational cost, further refinements are needed to address the shortcomings identified in this study so that these models can support all aspects of wind farm design and certification with confidence. Future work should include continued development, calibration, and validation of DWM models against high-fidelity benchmarks and field measurements under a broader range of operating conditions and more complex farm layouts. Additionally, controlled sensitivity studies are recommended to isolate the contributions of each DWM sub-modelling choice. By addressing the identified shortcomings, future DWM-based models will be able to more accurately represent complex wake interactions, thereby improving predictions of both energy yield and structural loads in large wind farms.

Author contributions. All authors: proposed the methodology, formal analysis, and investigation. ØWHB: simulated the test cases and submitted the $\mathrm{DWM_{IFE}}$ results. PD: simulated the test cases and submitted the $\mathrm{DWM_{NREL}}$ results. HAaM: simulated the test cases and submitted the $\mathrm{DWM_{DTU}}$ results. HA: Produced the LES inflow wind fields, simulated the test cases and submitted the $\mathrm{LES_{UU}}$ results. ØWHB: post-processed (except for the wake centre tracking) and visualized the data from the numerical models. PD: conducted the SAMWICh wake tracking and post-processing. ØWHB: wrote the manuscript draft. All authors: reviewed and edited the paper.

Competing interests. The authors declare that they have no conflict of interest.

Acknowledgements. This work has been funded by the Norwegian Research Council, through the project NEXTFARM: Engineering speed modelling of realistic fatigue for all the individual turbines in wind parks by representative pre-calculations, Grant No. 281020.

This work was authored in part by the National Renewable Energy Laboratory for the U.S. Department of Energy (DOE) under Contract No. DE-AC36-08GO28308. The views expressed in the article do not necessarily represent the views of the DOE or the U.S. Government. The U.S. Government retains and the publisher, by accepting the article for publication, acknowledges that the U.S. Government retains a nonexclusive, paid-up, irrevocable, worldwide license to publish or reproduce the published form of this work, or allow others to do so, for U.S. Government purposes.

References

Asmuth, H., Diaz, G. P. N., Madsen, H. A., Branlard, E., Forsting, A. R. M., Nilsson, K., Jonkman, J., and Ivanell, S.: Wind turbine response in waked inflow: A modelling benchmark against full-scale measurements, Renew. Energ., 191, 868–887, https://doi.org/10.1016/j.renene.2022.04.047, 2022.

Bartl, J., Mühle, F., Schottler, J., Sætran, L., Peinke, J., Adaramola, M., and Hölling, M.: Wind tunnel experiments on wind turbine wakes in yaw: effects of inflow turbulence and shear, Wind Energ. Sci., 3, 329–343, https://doi.org/10.5194/wes-3-329-2018, 2018.

Bernard, V., Andersen, S. J., Leon, J. M., Beaudet, L., Verelst, D., and Iliopoulos, A.: Observation and modelling of asymmetric loading on large offshore wind turbines in wake conditions, in: Journal of Physics: Conference Series, The Science of Making Torque from Wind, Florence, Italy, 29-31 May, 2024, 092092, vol. 2767, https://doi.org/10.1088/1742-6596/2767/9/092092, 2024.

Bossuyt, J., Scott, R., Ali, N., and Cal, R. B.: Quantification of wake shape modulation and deflection for tilt and yaw misaligned wind turbines, J. Fluid Mech., 917, A3, https://doi.org/10.1017/jfm.2021.237, 2021.

Branlard, E., Martínez-Tossas, L. A., and Jonkman, J.: A time-varying formulation of the curled wake model within the FAST.Farm framework, Wind Energy, 26, 44–63, https://doi.org/10.1002/we.2785, 2023.

Branlard, E., Jonkman, J., Platt, A., Thedin, R., Martínez-Tossas, L. A., and Kretschmer, M.: Development and Verification of an Improved Wake-Added Turbulence Model in FAST. Farm, in: Journal of Physics: Conference Series, The Science of Making Torque from Wind, Florence, Italy, 29-31 May, 2024, 092036, vol. 2767, https://doi.org/10.1088/1742-6596/2767/9/092036, 2024.

Clayton, B. R. and Filby, P.: Measured effects of oblique flows and change in blade pitch angle on performance and wake development of model wind turbines, in: Proceedings of the fourth BWEA Wind Energy Conference, BHRA Fluid Engineering, Cranfield, Bedford, UK, 214–224, 1982.

de Vaal, J. B. and Muskulus, M.: Simplified wake modelling for wind farm load prediction, in: Journal of Physics: Conference Series, EERA DeepWind'2021, Trondheim, Norway, 13-15 January 2021, 012012, IOP Publishing, https://doi.org/10.1088/1742-6596/2018/1/012012, 2021.

Doubrawa, P., Barthelmie, R. J., Wang, H., and Churchfield, M. J.: A stochastic wind turbine wake model based on new metrics for wake characterization, Wind Energy, 20, 449–463, https://doi.org/10.1002/we.2015, 2017.

Doubrawa, P., Annoni, J. R., and Jonkman, J. M.: Optimization-Based Calibration of FAST.Farm Parameters against SOWFA, 2018 Wind Energy Symposium, Kissimmee, Florida, USA, 8–12 January 2018, https://doi.org/10.2514/6.2018-0512, 2018.

Doubrawa, P., Shaler, K., and Jonkman, J.: Difference in load predictions obtained with effective turbulence vs. a dynamic wake meandering modeling approach, Wind Energ. Sci., 8, 1475–1493, https://doi.org/10.5194/wes-8-1475-2023, 2023.

Fleming, P. A., Gebraad, P. M., Lee, S., van Wingerden, J.-W., Johnson, K., Churchfield, M., Michalakes, J., Spalart, P., and Moriarty, P.: Evaluating techniques for redirecting turbine wakes using SOWFA, Renew. Energ., 70, 211–218, https://doi.org/10.1016/j.renene.2014.02.015, 2014.

Glauert, H.: Airplane Propellers, in: Aerodynamic Theory, Springer, Berlin, Heidelberg, Germany, 169–360, 1 edn., https://doi.org/10.1007/978-3-642-91487-4_3, 1935.

Hanssen-Bauer, W., De Vaal, J. B., Tutkun, M., Asmuth, H., Ivanell, S., and Stenbro, R.: Dependence of wind turbine loads on inlet flow field, in: Journal of Physics: Conference Series, Wind Energy Science Conference, Cork, Ireland, 17–20 June 2019, 062065, https://doi.org/10.1088/1742-6596/1618/6/062065, 2020.

Hanssen-Bauer, W., Doubrawa, P., Madsen, H. A., Asmuth, H., Jonkman, J., Larsen, G. C., Ivanell, S., and Stenbro, R.: Comparison of three DWM-based wake models at above-rated wind speeds, in: Journal of Physics: Conference Series, Wake Conference, Visby, Sweden, 20–22 June 2023, 012054, https://doi.org/10.1088/1742-6596/2505/1/012054, 2023.

International Electrotechnical Commision: Wind energy generation systems - Part 1: Design requirements, IEC 61400-1:2019, https://webstore.iec.ch/en/publication/26423, (last access: 5 February 2021), 2019.

Jonkman, J., Butterfield, S., Musial, W., and Scott, G.: Definition of a 5-MW reference wind turbine for offshore system development, Tech. Rep., National Renewable Energy Laboratory, Golden, CO, USA, 2009.

Jonkman, J., Doubrawa, P., Hamilton, N., Annoni, J., and Fleming, P.: Validation of FAST. Farm Against Large-Eddy Simulations, in: Journal of Physics: Conference Series, The Science of Making Torque from Wind, Milan, Italy, 20-22 June 2018, 062005, vol. 1037, https://doi.org/10.1088/1742-6596/1037/6/062005, 2018.

Jonkman, J. M., Annoni, J., Hayman, G., Jonkman, B., and Purkayastha, A.: Development of FAST. Farm: a new multi-physics engineering tool for wind-farm design and analysis, 35th Wind Energy Symposium, Grapevine, Texas, USA, 9-13 January 2017, 0454, https://doi.org/10.2514/6.2017-0454, 2017.

Keck, R.-E., Madsen, H. A., Larsen, G. C., Veldkamp, D., Wedel-Heinen, J. J., and Forsberg, J.: A consistent turbulence formulation for the dynamic wake meandering model in the atmospheric boundary layer, Ph.D. thesis, Technical University of Denmark, Lyngby, Denmark, 2013.

Keck, R.-E., de Maré, M., Churchfield, M. J., Lee, S., Larsen, G., and Madsen, H. A.: Two improvements to the dynamic wake meandering model: including the effects of atmospheric shear on wake turbulence and incorporating turbulence build-up in a row of wind turbines, Wind Energy, 18, 111–132, https://doi.org/10.1002/we.1686, 2015.

Larsen, G. C. and Lio, A. W.: Low-pass filtering of meandering scales, in: Journal of Physics: Conference Series, Wake Conference, Visby, Sweden, 10–12 June 2025, 012020, vol. 3016, p. 012020, https://doi.org/10.1088/1742-6596/3016/1/012020, 2025.

Larsen, G. C., Madsen, H. A., Thomsen, K., and Larsen, T. J.: Wake meandering: a pragmatic approach, Wind Energy, 11, 377–395, https://doi.org/10.1002/we.267, 2008.

Larsen, G. C., Ott, S., Liew, J., van der Laan, M. P., Simon, E., Thorsen, G. R., and Jacobs, P.: Yaw induced wake deflection - a full-scale validation study, in: Journal of Physics: Conference Series, The Science of Making Torque from Wind, Online, 28 September - 2 October, 2020, 062047, vol. 1618, IOP Publishing, https://doi.org/10.1088/1742-6596/1618/6/062047, 2020.

Larsen, T. J., Madsen, H. A., Larsen, G. C., and Hansen, K. S.: Validation of the dynamic wake meander model for loads and power production in the Egmond aan Zee wind farm, Wind Energy, 16, 605–624, https://doi.org/10.1002/we.1563, 2013.

Larsen, T. J., Larsen, G. C., Madsen, H. A., and Petersen, S. M.: Wake effects above rated wind speed. An overlooked contributor to high loads in wind farms, EWEA Annual Conference and Exhibition, Paris, France, 17 - 20 November 2015, 95–99, 2015.

Larsen, T. J., Larsen, G. C., Pedersen, M. M., Enevoldsen, K., and Madsen, H. A.: Validation of the Dynamic Wake Meander model with focus on tower loads, in: Journal of Physics: Conference Series, Wake Conference, Visby, Sweden, 30 May - 1 June 2017, 012027, https://doi.org/10.1088/1742-6596/854/1/012027, 2017.

Liew, J. and Larsen, G. C.: How does the quantity, resolution, and scaling of turbulence boxes affect aeroelastic simulation convergence?, in: Journal of Physics: Conference Series, The Science of Making Torque from Wind, Delft, Netherlands, 1-3 June 2022, 032049, vol. 2265, https://doi.org/10.1088/1742-6596/2265/3/032049, 2022.

Liu, L., Franceschini, L., Oliveira, D. F., Galeazzo, F. C., Carmo, B. S., and Stevens, R. J. A. M.: Evaluating the accuracy of the actuator line model against blade element momentum theory in uniform inflow, Wind Energy, 25, 1046–1059, https://doi.org/10.1002/we.2714, 2022.

Machefaux, E., Larsen, G. C., Troldborg, N., Hansen, K. S., Angelou, N., Mikkelsen, T., and Mann, J.: Investigation of wake interaction using full-scale lidar measurements and large eddy simulation, Wind Energy, 19, 1535–1551, https://doi.org/10.1002/we.1936, 2016.

Madsen, H. A., Larsen, G. C., and Thomsen, K.: Wake flow characteristics in low ambient turbulence conditions, Copenhagen Offshore Wind, Copenhagen, Denmark, 26-28 October 2005, 2005.

Madsen, H. A., Larsen, G. C., Larsen, T. J., Mikkelsen, R., and Troldborg, N.: Wake deficit-and turbulence simulated with two models compared with inflow measurements on a 2MW turbine in wake conditions, European Wind Energy Conference and Exhibition, Brussels, Belgium, 31 March – 3 April 2008, 48-53, 2008.

Madsen, H. A., Larsen, G. C., Larsen, T. J., Troldborg, N., and Mikkelsen, R.: Calibration and validation of the dynamic wake meandering model for implementation in an aeroelastic code, Journal of Solar Energy Engineering J. Sol. Energy Eng., 132, 041 014, https://doi.org/10.1115/1.4002555, 2010.

Madsen, H. A., Larsen, T. J., Larsen, G. C., and Hansen, K. S.: Wake flow characteristics at high wind speed, in: 34th Wind Energy Symposium, San Diego, California, USA, 4-8 January 2016, 1522, https://doi.org/10.2514/6.2016-1522, 2016.

Madsen, H. A., Larsen, T. J., Pirrung, G., Li, A., and Zahle, F.: Implementation of the Blade Element Momentum Model on a Polar Grid and its Aeroelastic Load Impact, Wind Energ. Sci., 5, 1–27, https://doi.org/10.5194/wes-2019-53, 2020.

Meyer Forsting, A. R., Pirrung, G. R., and Ramos-García, N.: A vortex-based tip/smearing correction for the actuator line, Wind Energ. Sci., 4, 369–383, https://doi.org/10.5194/wes-4-369-2019, 2019.

Michelsen, J. A.: Basis3D - a platform for development of multiblock PDE solvers, Tech. Rep., Technical University of Denmark, Lyngby, Denmark, 1994a.

Michelsen, J. A.: Block structured multigrid solution of 2D and 3D elliptic PDE's, Tech. Rep., Technical University of Denmark, Lyngby, Denmark, 1994b.

Monin, A. S., A. M. O.: Basic laws of turbulent mixing in the surface layer of the atmosphere, Nauk SSSR Geophiz. Inst, 24, 163–187, 1954.

NREL: OpenFAST, https://www.nrel.gov/wind/nwtc/openfast, last access: 22 August 2025, 2025.

Nygaard, T. A., De Vaal, J., Pierella, F., Oggiano, L., and Stenbro, R.: Development, verification and validation of 3DFloat; aero-servo-hydro-elastic computations of offshore structures, in: Journal of Physics: Conference Series, EERA DeepWind'2016, Trondheim, Norway, 20-22 January 2016, 425–433, vol. 94, https://doi.org/10.1016/j.egypro.2016.09.210, 2016.

RCN: Engineering speed modelling of realistic fatigue for all the individual turbines in wind parks by representative pre-calculations - Prosjektbanken, https://prosjektbanken.forskningsradet.no/project/FORISS/281020, last access: 25 August 2025, 2025.

Rychlik, I.: A new definition of the rainflow cycle counting method, Int. J. Fatigue, 9, 119–121, https://doi.org/10.1016/0142-1123(87)90054-5, 1987.

Shaler, K. and Jonkman, J.: FAST.Farm development and validation of structural load prediction against large eddy simulations, Wind Energy, 24, 428–449, https://doi.org/10.1002/we.2581, 2021.

Sood, I., Simon, E., Vitsas, A., Blockmans, B., Larsen, G. C., and Meyers, J.: Comparison of large eddy simulations against measurements from the Lillgrund offshore wind farm, Wind Energ. Sci., 7, 2469–2489, https://doi.org/10.5194/wes-7-2469-2022, 2022.

Sørensen, J. N. and Shen, W. Z.: Numerical modeling of wind turbine wakes, J. Fluids Eng., 124, 393–399, https://doi.org/10.1115/1.1471361, 2002.

Sørensen, N. N.: General purpose flow solver applied to flow over hills, Ph.D. thesis, Risø National Laboratory, Roskilde, Denmark, 1995.

Trujillo, J.-J., Bingöl, F., Larsen, G. C., Mann, J., and Kühn, M.: Light detection and ranging measurements of wake dynamics. Part II: two-dimensional scanning, Wind Energy, 14, 61–75, https://doi.org/10.1002/we.402, 2011.

Zong, H. and Porté-Agel, F.: A momentum-conserving wake superposition method for wind farm power prediction, J. Fluid Mech., 889, A8, https://doi.org/10.1017/jfm.2020.77, 2020a.

Zong, H. and Porté-Agel, F.: A point vortex transportation model for yawed wind turbine wakes, J. Fluid Mech., 890, A8, https://doi.org/10.1017/jfm.2020.123, 2020b.

Appendix A: Supplementary figures

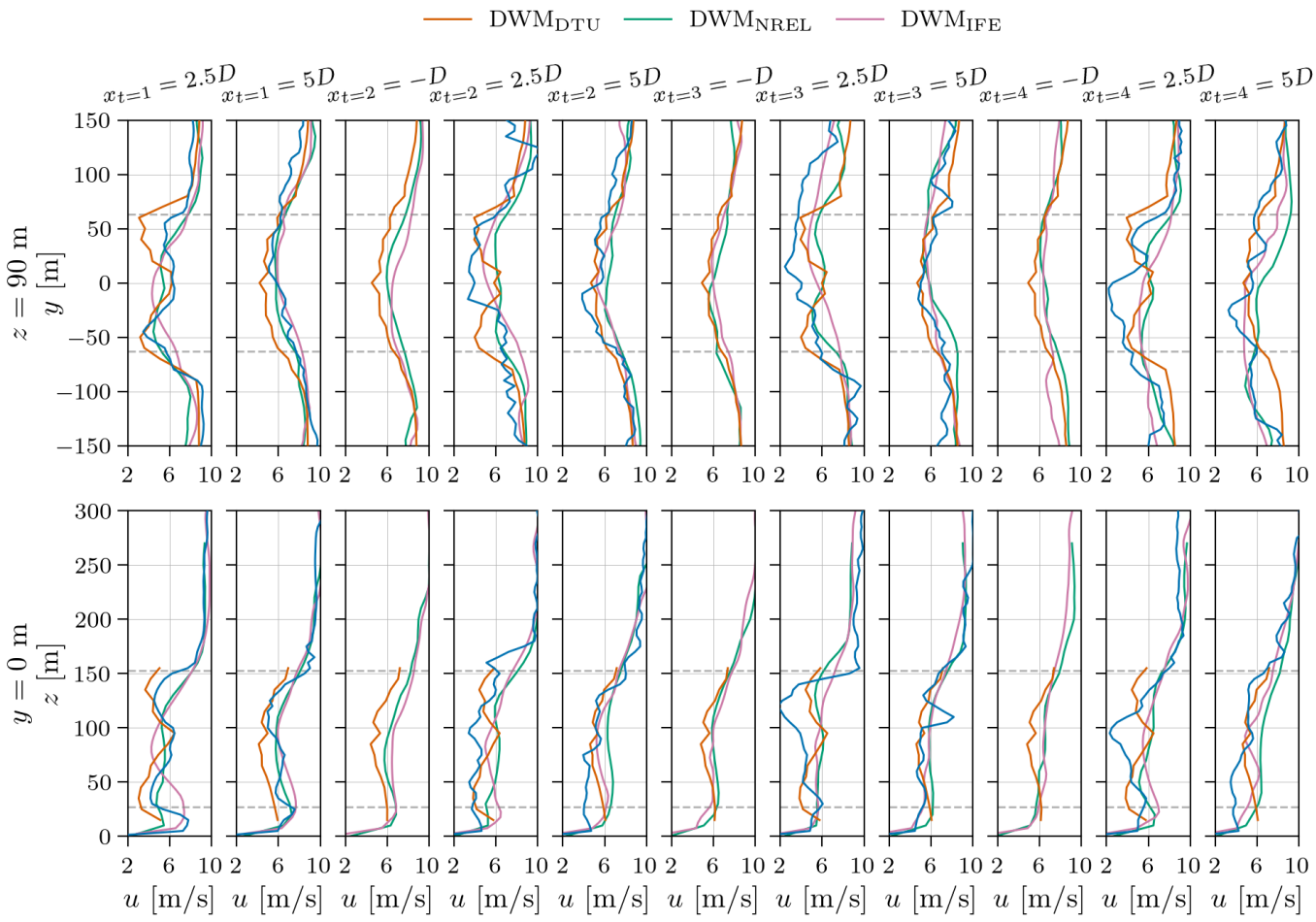

Figure A1. Instantaneous velocity profiles at t = 100 s for the aligned incoming wind case with low ambient turbulence (TI_a = 4.6 %). Horizontal dashed lines indicate the rotor swept area. LES_{UU} is missing at $x_{t=i} = -D,\ i = 2, 3, 4$ due to lack of time-resolved data at this axial position.

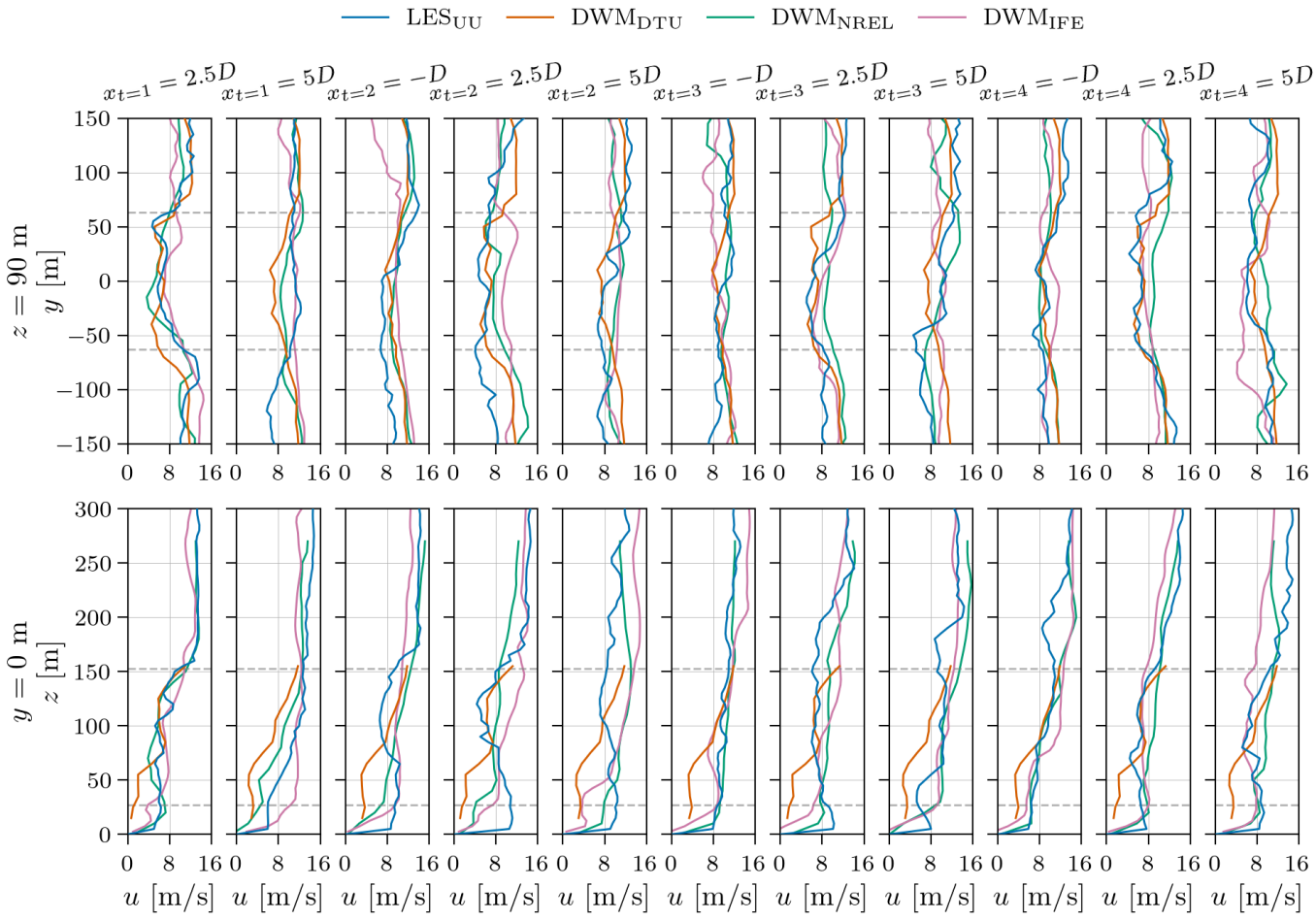

Figure A2. Instantaneous velocity profiles at t = 100 s for the aligned incoming wind case with high ambient turbulence (TI_a = 12.0 %). Horizontal dashed lines indicate the rotor swept area.

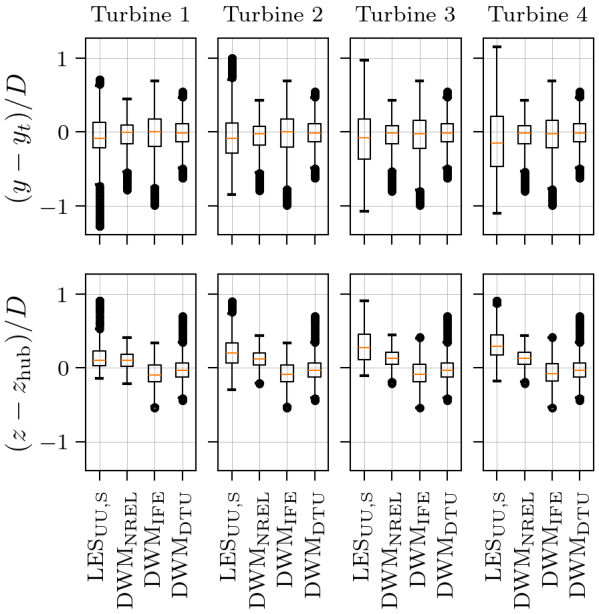

Figure A3. Box plots of horizontal (upper row) and vertical (lower row) wake centre positions at $x = 5D$ behind the turbines, for the aligned incoming wind case with medium ambient turbulence ($\mathrm{TI_a}$ = 8.8 %).

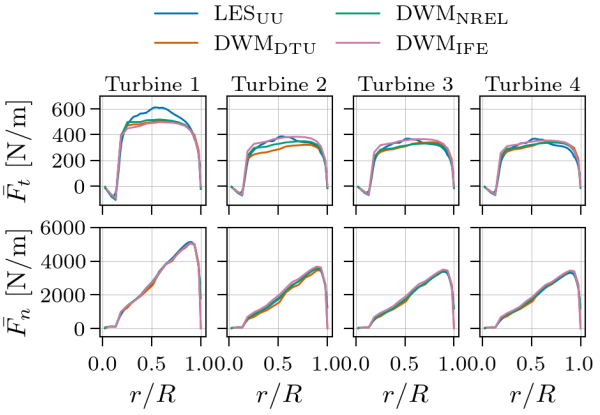

Figure A4. Time-averaged blade force as function of blade radius for the aligned incoming wind case with medium ambient turbulence ($\mathrm{TI_a}$ = 8.8 %).

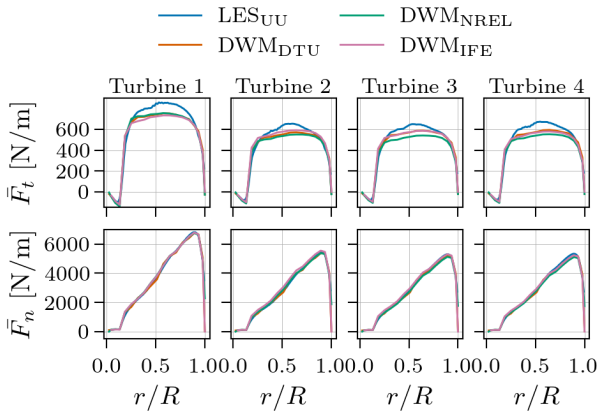

Figure A5. Time-averaged blade force as function of blade radius for the aligned incoming wind case with high ambient turbulence (TI_a = 12 %).

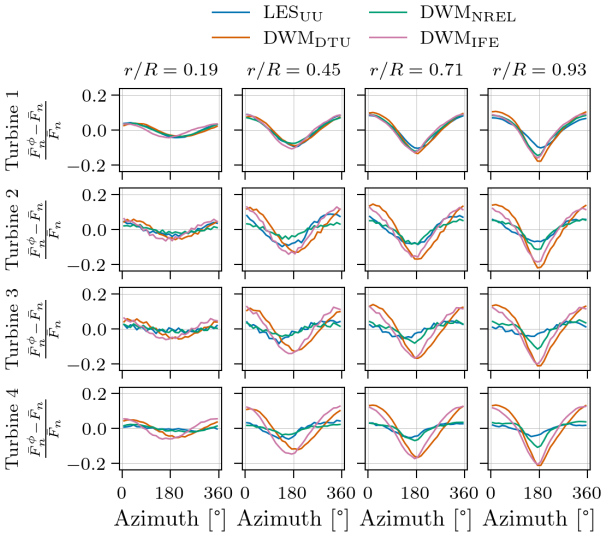

Figure A6. Relative difference between mean normal blade force per azimuthal bin $\bar{F}_n^\phi$ and total normal force $\bar{F}_n$, for TI_a = 8.8 %.

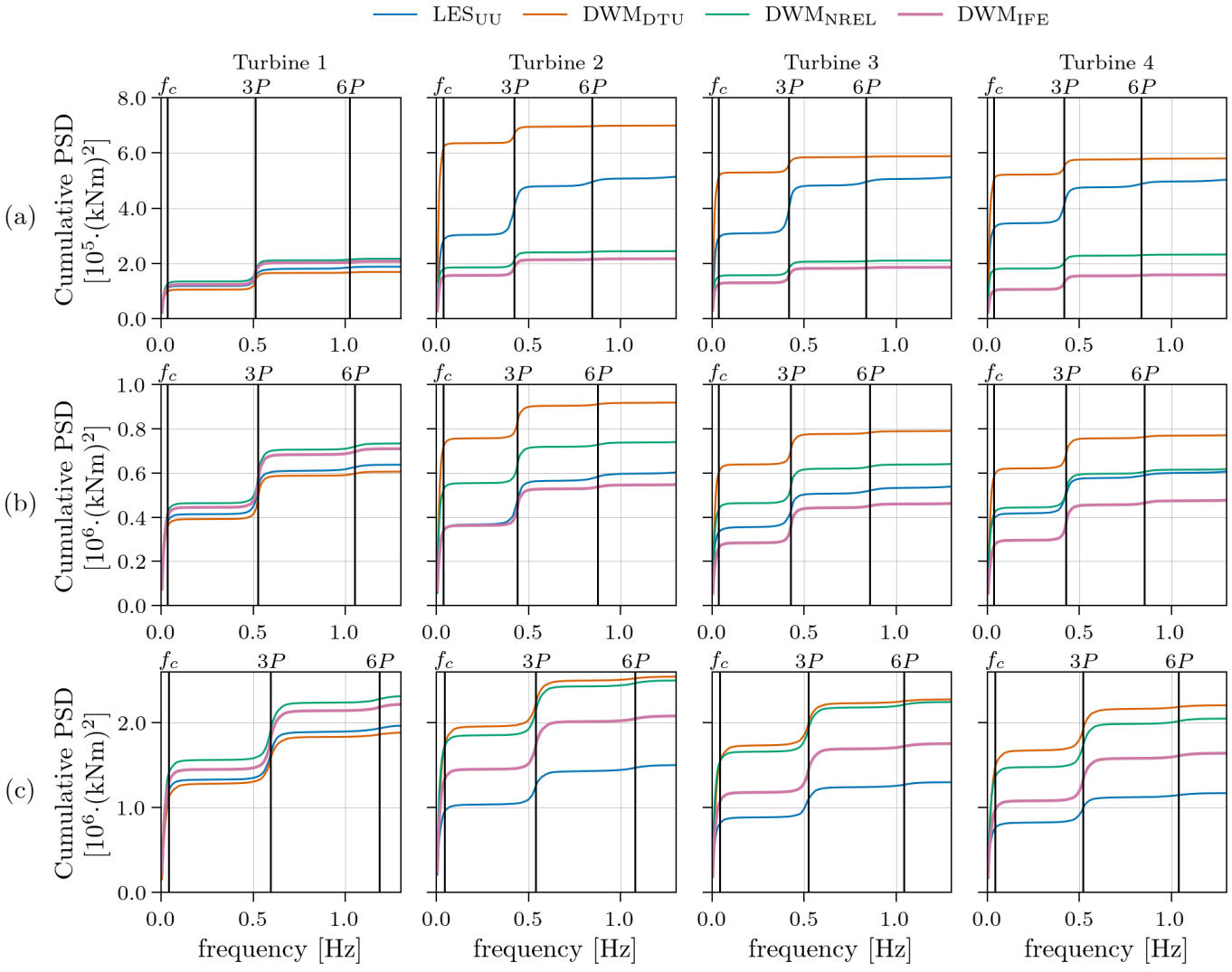

Figure A7. Energy spectra of tower-top yaw moment for the aligned incoming wind case with ambient turbulence of (a) TI_a = 4.6 %, (b) TI_a = 8.8 %, and (c) TI_a = 12 %.

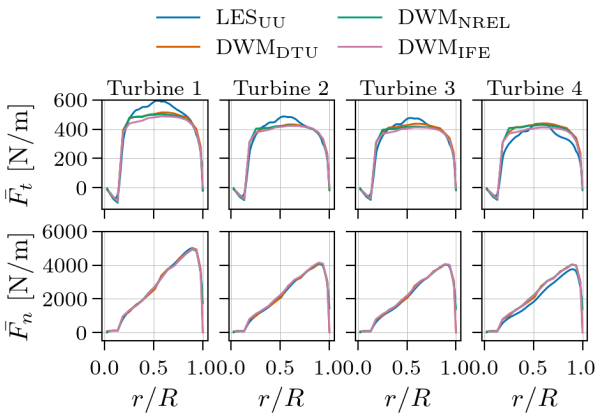

Figure A8. Time-averaged blade force as function of blade radius for the partially waked case, 5° inflow angle and medium ambient turbulence (TI_a = 8.8 %).

Appendix B: Aeroelastic solver sensitivity analysis

Since the inflow to turbine 1 is identical across all models, any differences in response for this turbine likely originate from the aeroelastic solvers to which the different wake models are coupled, rather than from the wake models themselves – the primary focus of this study. Ideally, to isolate the impact of the wake models, all simulations should be performed using the same aeroelastic solver. However, this would require code modifications ~~and rerunning the simulations~~.

Alternatively, if the discrepancies between the aeroelastic solvers are consistent across wind speeds, the solver effect can be mitigated by normalizing all turbine outputs by the value of turbine 1. To test this assumption ~~with minimal additional simulations~~, the flow fields from $\mathrm{DWM_{NREL}}$ and $\mathrm{DWM_{IFE}}$ at $x_t = -D$ were converted and used as input to 3DFloat, the aeroelastic solver from IFE. The resulting mean thrust force and aerodynamic power are shown in Fig. B1 for the aligned inflow case with medium ambient turbulence ($\mathrm{TI_a}$ = 8.8 %). The original results from $\mathrm{DWM_{NREL}}$ and $\mathrm{DWM_{IFE}}$ are also included for comparison.

As expected, thrust and power outputs for turbine 2–4 are lower in the simulations using flow fields at $x_t = -D$, compared to the original simulations where the inflow has recovered for $1D$ longer. However, while the original $\mathrm{DWM_{NREL}}$ results were generated using NREL's aeroelastic solver OpenFAST, the three other simulations all used 3DFloat. Because the reductions in thrust and power between the simulations using the wake model by NREL and for the simulations using the wake model by IFE are similar, we can conclude that the aeroelastic solvers have a negligible effect on the ~~reduced~~ results.

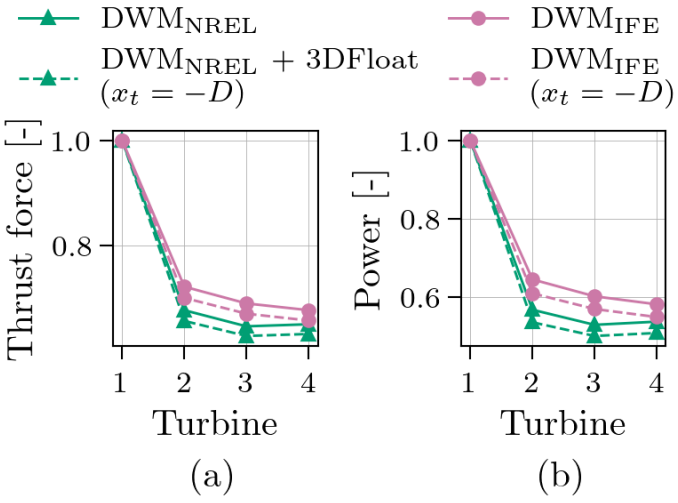

Figure B1. (a) Mean thrust force and (b) mean power for the aligned incoming wind case with medium ambient turbulence ($\mathrm{TI_a}$ = 8.8 %). For each model, the thrust and power outputs are normalized by the value of turbine 1.

Similarly, the DELs of the blade-root flapwise bending moment, tower-top yaw moment, and tower-base fore-aft bending moment are shown in Fig. B2 for both the new and original simulations. Here, the DELs for turbine 2-4 are higher in the

simulations using the flow fields at $x_t = -D$, as expected, since the inflow in the original simulations has recovered for $1D$ longer and become less turbulent. Also for the DELs, the reductions are similar for the simulations using the wake model by NREL and for the simulations using the wake model by IFE, even though some slightly larger deviations are observed than for the mean values. Still, it seems like an acceptable conclusion that also for the fatigue damage the aeroelastic solvers have a negligible effect on the results when normalized by the value of turbine 1.

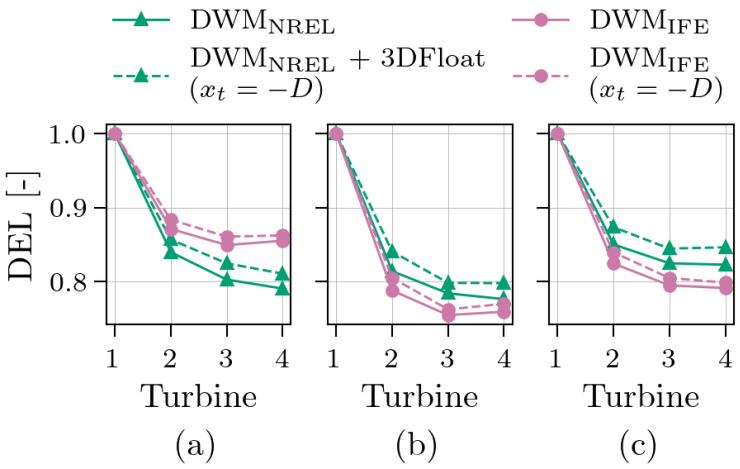

Figure B2. Fatigue of (a) blade-root flapwise bending moment, (b) tower-top yaw moment, and (c) tower-base fore-aft bending moment for the aligned incoming wind case with medium ambient turbulence (TI_a = 8.8 %). For each model, the DELs are normalized by the DEL of turbine 1.